PIONEER AND INNOVATIVE STUDIES IN ELECTRICAL, ELECTRONIC AND COMMUNICATION ENGINEERING

All Sciences Academy

PIONEER AND INNOVATIVE STUDIES IN ELECTRICAL, ELECTRONIC AND COMMUNICATION ENGINEERING

Editor

Assoc. Prof. Dr. Doğan ÇELİK

Pioneer and Innovative Studies In Electrical, Electronic and Communication Engineering

Editor: *Assoc. Prof. Dr. Doğan ÇELİK*

Design: All Sciences Academy Design
Published Date: December 2024
Publisher's Certification Number: 72273
ISBN: 978-625-5954-14-5

www.allsciencesacademy.com
allsciencesacademy@gmail.com

CONTENT

Investigating the Application Of AC-AC Conversion Techniques Through Matrix Converters to Linear Asynchronous Motors

Mehmet Latif LEVENT[1]

1- Assistant Professor, Hakkari University, Faculty of Engineering, Department of Electrical-Electronics. mehmetlatiflevent@hakkari.edu.tr ORCID No: 0000-0002-7185-9029

ABSTRACT

Matrix converters have emerged as a pivotal advancement in the field of power electronics, eliminating the need for capacitors for energy storage through direct AC-AC conversion. These devices utilize a matrix arrangement of nine semiconductor switching elements, each controlling a phase, to facilitate direct and efficient power transfer between input and output. This innovative structure not only allows for effective control over the input power factor and enables bidirectional power flow but also ensures that both the input and output waveforms remain sinusoidal. This study delves into the reasons behind the preference for Insulated Gate Bipolar Transistors (IGBTs) in matrix converters, particularly in applications involving high current and voltage. It thoroughly examines the advantages offered by IGBTs in terms of switching speed, losses, and ease of control. Advanced control techniques such as the Venturini Modulation Algorithm are explored for adjusting the output voltage and frequency of matrix converters to desired levels. This algorithm ensures the maintenance of sinusoidal waveforms for both input currents and output voltage, allowing the output voltage amplitude to achieve up to 86.6% of the input voltage amplitude. The theoretical discussions are supplemented with a simulation study conducted using Matlab/Simulink, demonstrating the matrix converter's capability to feed a load with a specified amplitude and frequency. The simulation results illustrate how a Linear Induction Motor (LIM) can be effectively powered to meet specific targets, showcasing variations in the motor's thrust force and speed.

Keywords – Linear Induction Motor, Matlab/Simulink, Matrix Converters, Power Electronics, Venturini Modulation Algorithm.

INTRODUCTION

The industrial application of asynchronous motors necessitates the provision of voltages varying in frequency and amplitude. This requirement is traditionally met by AC-DC-AC converters or AC-AC converters. These converters play a pivotal role in adapting the power supply to meet the specific demands of various industrial loads. The AC-DC-AC conversion process involves rectifying the alternating current (AC) to direct current (DC), followed by an inversion back to AC with desired characteristics. On the other hand, AC-AC converters facilitate a more direct conversion, altering the waveform of the input AC power to match the required output specifications (Wijesekera et al., 2023).

The ability to supply voltages with variable frequencies and amplitudes is crucial for the optimal performance of asynchronous motors in

different industrial settings. This flexibility enables precise control over motor speed and torque, enhancing the efficiency and effectiveness of various industrial processes. The advancements in semiconductor technology have been instrumental in developing converters capable of providing these specific voltage requirements, thereby broadening the scope of applications for asynchronous motors (Bose, 2020).

Matrix converters represent a groundbreaking development in the field of power electronics, offering a more efficient method for AC-AC conversion. Unlike traditional converters, matrix converters do not require reactive energy storage components, such as capacitors and inductors, for their operation. This innovative approach enables the direct conversion of input AC power to a desired output AC waveform without intermediate DC stages. The fundamental principle of matrix converters is based on the cycloconverter concept, which allows for the direct modulation of input voltage phases to achieve the required output.

The concept of matrix converters was first introduced in 1976 by Gyugyi and Pelly. Their pioneering work laid the foundation for modern matrix converter designs, utilizing the cycloconverter principle. This initial design, however, encountered challenges related to the generation of harmonics in the input current and output voltage, which could not be easily mitigated through filtering (Friedli, and Kolar., 2012).

The introduction of a new control algorithm by Venturini marked a significant advancement in overcoming the harmonic issues associated with early matrix converters. This innovative control strategy enabled the effective suppression of undesirable harmonics, ensuring smoother and more efficient operation. The adoption of Venturini's algorithm has been instrumental in enhancing the performance and reliability of matrix converters, making them a viable alternative for industrial applications requiring AC-AC conversion (Varajao and Araújo, 2021).

Matrix converters offer several advantages over traditional conversion technologies, making them increasingly popular in industrial applications. Their ability to operate without energy storage intermediate elements leads to a more compact and efficient design. Additionally, matrix converters facilitate sinusoidal input and output currents and allow for independent power factor control, irrespective of the load. However, these benefits come with certain challenges. The complexity of their topology and the increased number of components can make implementation more difficult and raise switching losses.

Looking forward, the role of matrix converters in asynchronous motor drive systems is set to expand. Their efficiency, combined with the growing need for energy-saving technologies and precise motor control, positions them as a key component in future industrial applications. Continued research and development are expected to further enhance their performance

and reduce the associated challenges, paving the way for broader adoption in a variety of industrial settings.

As technology continues to advance, the potential applications for asynchronous motors and matrix converters are likely to extend beyond current industrial uses, contributing to more innovative and energy-efficient solutions across multiple sectors.

THE STRUCTURE OF THE MATRİX CONVERTER

Matrix converters have emerged as a significant technological advancement in the field of power electronics, offering direct AC-AC conversion without the need for capacitors for energy storage. This is attributed to the absence of a rectifier unit in their design. The ability of matrix converters to operate efficiently across four quadrants with respect to the speed-torque characteristic endows them with a distinct advantage in motor feeding applications over other types of converters (Bento et al., 2021).

A matrix converter is a sophisticated device that performs direct AC-AC conversion. This innovative design negates the need for capacitors for energy storage, a typical requirement in conventional converters. The absence of a rectifier unit is a key characteristic that distinguishes matrix converters from other converter types. The interest in matrix converters has surged, primarily due to their ability to produce sinusoidal input and output waveforms, control input power factor effectively, and facilitate bidirectional power flow through the use of switches that allow current flow in both directions (Mahmud and Gao 2024,).

The matrix converter is constructed through the strategic arrangement of bidirectional semiconductor switching elements placed in a matrix format between the input and output terminals. In the context of a 3-phase AC-AC matrix converter, there are nine semiconductor switching elements in total, with three dedicated to each phase. This configuration is instrumental in the converter's functionality, allowing for the precise control of power transfer between the input and output.

The generation of a single-phase output voltage from a matrix converter involves the appropriate manipulation of the 3-phase input voltages via semiconductor switches. By meticulously adjusting the conduction times of these switches, it is possible to achieve the desired amplitude and frequency of the output voltage. The output voltage's sinusoidal waveform is a direct function of the magnitude of the switching frequency, underscoring the importance of switch control in matrix converter operations (Ishaq et al., 2021).

The connection of the semiconductor switching elements is shown in Figure 1. The output voltage of each phase is obtained by transferring each

input phase's voltage to the output in a regular sequence for a fixed switching period using the appropriate semiconductor switches. Each Sij switch shown in the figure is a bidirectional semiconductor switch. The indices used in the nomenclature of the switches indicate the input (i = A, B, C) and output (j = a, b, c) terminals. The same notation is also used to indicate the duration of the conduction period of the switches.

This paper delves into the operational intricacies of matrix converters, focusing particularly on the conduction durations of specific semiconductor switches and their impact on the output phase voltages. It further explores the preference for Insulated Gate Bipolar Transistors (IGBTs) in high-current and voltage applications, highlighting their advantages in terms of switching speed, losses, and ease of control.

In matrix converters, the conduction time of switches plays a crucial role in determining the output voltage characteristics. For instance, the conduction duration of the switch SAa, which transmits the A-phase input to the A-phase output, is denoted as tAa.

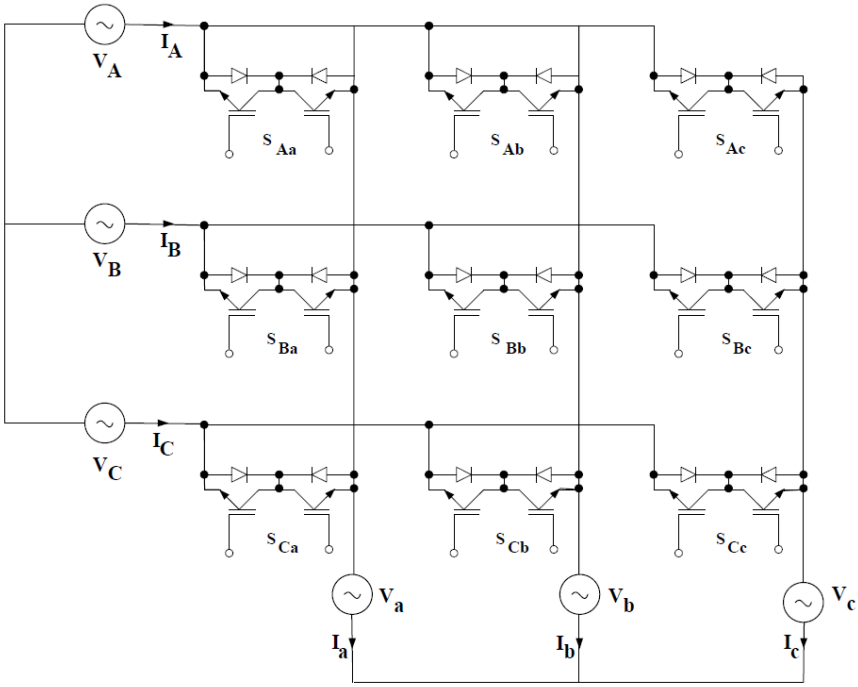

Figure 1: Three-phase matrix converter switch arrays

The formation of the Va output phase in a matrix converter, as depicted in Figure 1, is contingent on the conduction times of the switches. The VA phase is transmitted to the output during the conduction of SAa for a duration of tAa, followed by the VB phase through SBa for tBa, and finally the Vc phase via SCa for tCa. Consequently, the Va output voltage is derived

by appropriately clipping the VA, VB, VC input voltages. It is crucial to note that the sum of tAa, tBa, and tCa equals the fixed switching period.

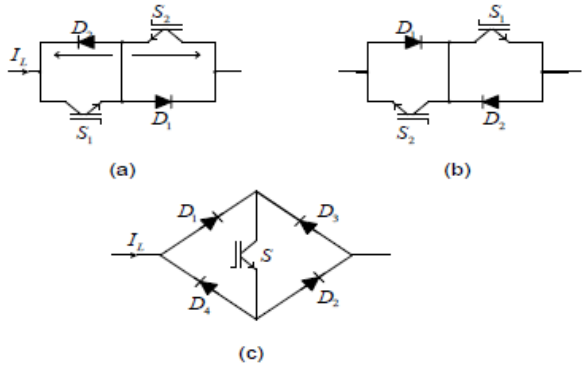

Figure 2: Bidirectional switching structures

In high-current and voltage applications, Insulated Gate Bipolar Transistors (IGBTs) are often favored over MOSFETs in power circuits. IGBTs amalgamate the advantages of easy driving, rapid operation, and robustness found in power MOSFETs, while also exhibiting low switching and conduction losses. Although the switching speed of an IGBT is relatively slower compared to a MOSFET, its lower switching losses make it increasingly preferred in medium power applications such as DC and AC motor drivers and controlled power sources. The growing adoption of IGBTs as switching elements in these applications is a testament to their efficiency and effectiveness (Töchterle, 2022).

Matrix converters necessitate the use of bidirectional switches, which are capable of conducting current in both directions and blocking reverse voltages. Currently, there is no single switching element available that inherently possesses these specific characteristics. Consequently, there is a need to employ a combination of different switching elements to form appropriate switch cells for matrix converters. Figure 2. illustrates the most commonly preferred switch structures in matrix converters. These bidirectional semiconductor switches are typically implemented using Insulated Gate Bipolar Transistors (IGBTs). The configuration of these bidirectional switches using IGBTs is a crucial aspect of matrix converter design, reflecting the need to effectively manage power flow and voltage reversal.

Venturini Modulation Algorithm

In 1980, Venturini introduced a new pulse-width modulation control algorithm for matrix converters. This algorithm allows for the achievement of desired amplitude and frequency levels in the output, ensuring that both input currents and output voltage maintain a sinusoidal waveform. Initially,

this control method allowed the output voltage amplitude to reach up to 50% of the input voltage amplitude. However, subsequent research by Venturini and Alesina increased this limit to 86.6% (Pipolo et. al, 2021).

Modulation in matrix converters is used to generate appropriate switching signals for each of the nine switches. This process involves the creation of a modulation matrix using the direct transfer function approach method. The primary goal of modulation is to produce variable frequency and amplitude sinusoidal output voltages from fixed frequency and amplitude input voltages.

Input and Output Voltages

During the modulation process in matrix converters, it is assumed that the switches operate ideally. Additionally, the voltages applied to the input of the matrix converter are considered to be balanced, three-phase sinusoidal voltages. Under these assumptions, the input voltage to the matrix converter is referred to as V_{ABC}, and the output voltage obtained from the matrix converter is denoted as V_{abc}.

These assumptions are important for simplifying the analysis and understanding of the modulation process in matrix converters, allowing for a clearer evaluation of their performance and operational characteristics.

$$V_{abc} = [m] V_{ABC} \tag{1}$$

Here, the matrix [m] is referred to as the modulation coefficient matrix which dictates the modulation process within the matrix converter.

$$V_{ABC} = \left[V_A V_B V_C\right]^T \; and \; V_{abc} = \left[V_a V_b V_c\right]^T \tag{2}$$

If the expression in Equation (2) is written more clearly;

$$\begin{bmatrix} V_a \\ V_b \\ V_c \end{bmatrix} = \begin{bmatrix} m_{Aa} & m_{Ba} & m_{Ca} \\ m_{Ab} & m_{Bb} & m_{Cb} \\ m_{Ac} & m_{Bc} & m_{Cc} \end{bmatrix} \begin{bmatrix} V_A \\ V_B \\ V_C \end{bmatrix} \tag{3}$$

It is possible to reveal the relationship between input and output voltages as follows. If the period of the switching frequency (f_s) is Ts, it is possible to express the relationship between the switching period of the modulation coefficient matrix [*m*] elements and the transmission time of the switches as follows.

$$\begin{bmatrix} m_{Aa} & m_{Ba} & m_{Ca} \\ m_{Ab} & m_{Bb} & m_{Cb} \\ m_{Ac} & m_{Bc} & m_{Cc} \end{bmatrix} = \frac{1}{T_S} \begin{bmatrix} t_{Aa} & t_{Ba} & t_{Ca} \\ t_{Ab} & t_{Bb} & t_{Cb} \\ t_{Ac} & t_{Bc} & t_{Cc} \end{bmatrix} \tag{4}$$

$$\begin{bmatrix} m_{Aa} & m_{Ba} & m_{Ca} \\ m_{Ab} & m_{Bb} & m_{Cb} \\ m_{Ac} & m_{Bc} & m_{Cc} \end{bmatrix} = \begin{bmatrix} 1 \\ 1 \\ 1 \end{bmatrix} \; and \; \begin{bmatrix} t_{Aa}+t_{Ba}+t_{Ca} \\ t_{Ab}+t_{Bb}+t_{Cb} \\ t_{Ac}+t_{Bc}+t_{Cc} \end{bmatrix} = \begin{bmatrix} T_S \\ T_S \\ T_S \end{bmatrix} \tag{5}$$

Considering that the phase sequence for input-output voltages is A-B-C or a-b-c, the following equations can be written between the terms of the modulation coefficient matrix or the transmission duration of the switches.

$$\begin{bmatrix} m_{Aa} \\ m_{Ba} \\ m_{Ca} \end{bmatrix} = \begin{bmatrix} m_{Bb} \\ m_{Cb} \\ m_{Ab} \end{bmatrix} = \begin{bmatrix} m_{Cc} \\ m_{Ac} \\ m_{Bc} \end{bmatrix} \; and \; \begin{bmatrix} t_{Aa} \\ t_{Ba} \\ t_{Ca} \end{bmatrix} = \begin{bmatrix} t_{Bb} \\ t_{Cb} \\ t_{Ab} \end{bmatrix} = \begin{bmatrix} t_{Cc} \\ t_{Ac} \\ t_{Bc} \end{bmatrix} \tag{6}$$

Therefore, to derive analytical expressions regarding the transmission time of the switches, a result can be written in a simpler form than equations (3), (4), (5) as follows.

$$\begin{bmatrix} V_a \\ V_b \\ V_c \end{bmatrix} = \begin{bmatrix} m_{Aa} & m_{Ba} & m_{Ca} \\ m_{Cb} & m_{Ab} & m_{Cb} \\ m_{Bc} & m_{Cc} & m_{Ac} \end{bmatrix} \begin{bmatrix} V_A \\ V_B \\ V_C \end{bmatrix} = \frac{1}{T_S} \begin{bmatrix} t_{Aa} & t_{Ba} & t_{Ca} \\ t_{Cb} & t_{Ab} & t_{Bb} \\ t_{Bc} & t_{Cc} & t_{Ac} \end{bmatrix} \begin{bmatrix} V_A \\ V_B \\ V_C \end{bmatrix} \tag{7}$$

Since sinusoidal 3-phase input voltages yield sinusoidal output 3-phase voltages with the desired amplitude and frequency, it is possible to write the input-output voltages as follows.

$$\begin{bmatrix} V_A \\ V_B \\ V_C \end{bmatrix} = V_{im} \begin{bmatrix} \cos(\omega_i t) \\ \cos(\omega_i t - 2\pi/3) \\ \cos(\omega_i t + 2\pi/3) \end{bmatrix} \; and \; \begin{bmatrix} V_a \\ V_b \\ V_c \end{bmatrix} = V_{om} \begin{bmatrix} \cos(\omega_o t) \\ \cos(\omega_o t - 2\pi/3) \\ \cos(\omega_o t + 2\pi/3) \end{bmatrix} \tag{8}$$

Here V_{im} and w_i are the peak value and frequency of the constant input voltage, respectively. V_{om} and w_o are the variable peak value and variable frequency of the output voltage. If equation (8) is substituted into Equation (7) with $q=V_{om}/V_{im}$ (demand factor), the following results can be obtained.

$$T_s q \begin{bmatrix} \cos(\alpha_0) \\ \cos(\beta_0) \\ \cos(\gamma_0) \end{bmatrix} = \begin{bmatrix} \cos(\alpha_i)\cos(\beta_i)\cos(\gamma_i) \\ \cos(\beta_i)\cos(\gamma_i)\cos(\alpha_i) \\ \cos(\gamma_i)\cos(\alpha_i)\cos(\beta_i) \end{bmatrix} \begin{bmatrix} t_{Aa} \\ t_{Ba} \\ t_{Ca} \end{bmatrix} \tag{9}$$

Within the context of matrix converters, the variables 'α_0', 'β_0', 'γ_0', and 'αi', 'β_i', 'γ_i' are defined in a manner represented by Eq. (10).

$$\begin{bmatrix} \alpha_0 \\ \beta_0 \\ \gamma_0 \end{bmatrix} = \begin{bmatrix} \omega_o t \\ \omega_o t - 2\pi/3 \\ \omega_o t + 2\pi/3 \end{bmatrix} \; and \; \begin{bmatrix} \alpha_i \\ \beta_i \\ \gamma_i \end{bmatrix} = \begin{bmatrix} \omega_i t \\ \omega_i t - 2\pi/3 \\ \omega_i t + 2\pi/3 \end{bmatrix} \tag{10}$$

From Equation (10), the expressions found in the first two rows, along with the first row from the matrix equation related to the switching times in Equation (5), can be utilized to derive analytical results for the durations t_{Aa},t_{Ba}, and t_{Ca}.

$$\begin{bmatrix} \cos(\alpha_i) & \cos(\beta_i) & \cos(\gamma_i) \\ \cos(\beta_i) & \cos(\gamma_i) & \cos(\alpha_i) \\ 1 & 1 & 1 \end{bmatrix} \begin{bmatrix} t_{Aa} \\ t_{Ba} \\ t_{Ca} \end{bmatrix} = T_s \begin{bmatrix} q\cos(\alpha_0) \\ q\cos(\beta_0) \\ 1 \end{bmatrix} \tag{11}$$

If this last set of equations is solved by accepting the switching times t_{Aa}, t_{Ba}, t_{Ca} as unknowns;

$$\begin{bmatrix} t_{Aa} \\ t_{Ba} \\ t_{Ca} \end{bmatrix} = \frac{T_A}{3} \begin{bmatrix} 1+2q\cos(\omega_m t) \\ 1+2q\cos(\omega_m t+2\pi/3) \\ 1+2q\cos(\omega_m t-2\pi/3) \end{bmatrix} \tag{12}$$

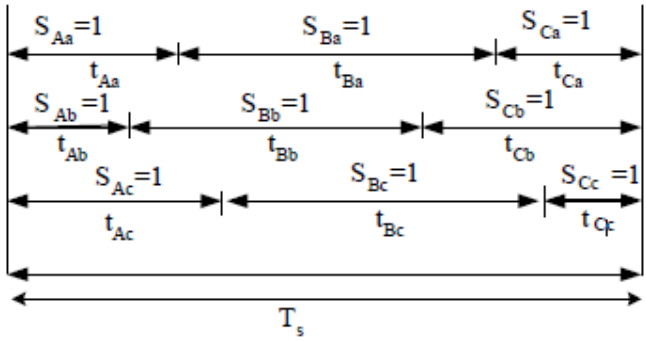

Figure 3: Triggering order of switches and their transmission time

In equation (12), it is possible to understand what the remaining switching times t_{Ab}, t_{Bb}, t_{Cb} and t_{Ac}, t_{Bc}, t_{Cc} and the modulation terms m_{Ab}, m_{Bb}, m_{Cb} and m_{Ac}, m_{Bc}, m_{Cc} will be by looking at equation (6).

To further elucidate this modulation technique, one can illustrate the conduction durations of the semiconductor switching elements for a single period of the switching frequency, as depicted in Figure 3. This visualization is instrumental in understanding the timing sequences that the matrix converter employs during operation.

Input and Output Currents

The objective of utilizing a matrix converter is to produce an output voltage with variable frequency from a constant sinusoidal input voltage. When the output voltages derived from this input are sinusoidal in nature, the output currents connected to the load of the matrix converter should also be sinusoidal, dependent on the characteristics of the load itself.

$$\begin{bmatrix} I_a \\ I_b \\ I_c \end{bmatrix} = I_{om} \begin{bmatrix} \cos(\omega_o t + \varphi) \\ \cos(\omega_o t + \varphi - 2\pi/3) \\ \cos(\omega_o t + \varphi + 2\pi/3) \end{bmatrix} \tag{14}$$

Here, ϕ is the power angle. As seen in Figure 3.4, the input currents I_A, I_B, I_C should be synthesized from the output currents I_a, I_b, I_c.

$$\begin{bmatrix} I_A \\ I_B \\ I_C \end{bmatrix} = \begin{bmatrix} I_{aA} & I_{aB} & I_{aC} \\ I_{bA} & I_{bB} & I_{bC} \\ I_{cA} & I_{cB} & I_{cC} \end{bmatrix} \tag{15}$$

The components of these output currents can also be expressed in terms of the output currents and modulation terms as follows.

$$\begin{bmatrix} I_{aA} \\ I_{aB} \\ I_{aC} \end{bmatrix} = \begin{bmatrix} m_{Aa} & m_{Ca} & m_{Ba} \end{bmatrix} \begin{bmatrix} I_a \\ I_b \\ I_c \end{bmatrix} \tag{16}$$

$$\begin{bmatrix} I_{bA} \\ I_{bB} \\ I_{bC} \end{bmatrix} = \begin{bmatrix} m_{Ba} & m_{Aa} & m_{Ca} \end{bmatrix} \begin{bmatrix} I_a \\ I_b \\ I_c \end{bmatrix} \tag{17}$$

$$\begin{bmatrix} I_{cA} \\ I_{cB} \\ I_{cC} \end{bmatrix} = \begin{bmatrix} m_{Ca} & m_{Ba} & m_{Aa} \end{bmatrix} \begin{bmatrix} I_a \\ I_b \\ I_c \end{bmatrix} \tag{18}$$

If equations (16), (17), and (18) are substituted into equation (15);

$$\begin{bmatrix} I_A \\ I_B \\ I_C \end{bmatrix} = \begin{bmatrix} m_{Aa} & m_{cA} & m_{Ba} \\ m_{Ba} & m_{Aa} & m_{Ca} \\ m_{Ca} & m_{Ba} & m_{Aa} \end{bmatrix} \begin{bmatrix} I_a \\ I_b \\ I_c \end{bmatrix} \tag{19}$$

It is observed that the input currents of the matrix converter are equal to the product of the transpose of the modulation coefficient matrix and the output currents. Therefore, in a very general expression, the input currents will be as indicated in equation (20).

$$I_{ABC} = \left[m\right]^T I_{abc} \tag{20}$$

Here, $I_{ABC}=[I_A,I_B,I_C]$, $I_{abc}=[I_a,I_b,I_c]$, and $[m]$ are the transpose of the modulation coefficient matrix. After equations (13) and (14) are substituted into equation (19), and after performing some algebraic manipulations, the

following analytical result expression related to the output currents I_a, I_b, I_c is derived.

$$\begin{bmatrix} I_A \\ I_B \\ I_C \end{bmatrix} = qI_{om} \begin{bmatrix} \cos(\omega_o t + \varphi) \\ \cos(\omega_o t + \varphi - 2\pi/3) \\ \cos(\omega_o t + \varphi + 2\pi/3) \end{bmatrix} \tag{21}$$

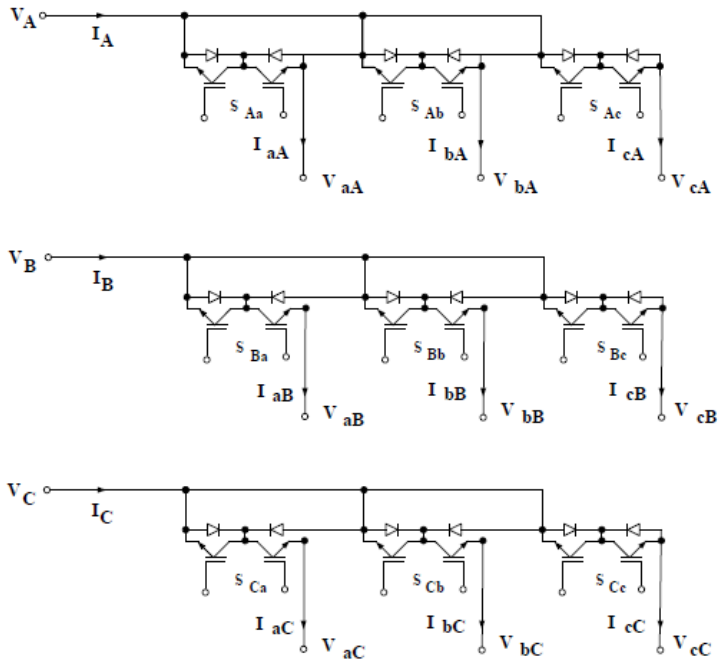

Figure 4: The input currents for each phase and the components of the output current

SIMULATION OF MATRIX CONVERTER USING MATLAB/SIMULINK

To simulate the Matrix Converter feeding the load within the limits allowed by the modulation algorithm in terms of amplitude and frequency, it is necessary to first measure any two line voltages of the three-phase source that will supply the converter, as shown in Figure 5. For instance, the voltages VAB and VBC have been measured here. In this modeling, a block named "Lineer Motor" is used as the load.The texts in the text should be 11 points and normal. If there are places that need special attention, italic fonts can be used.

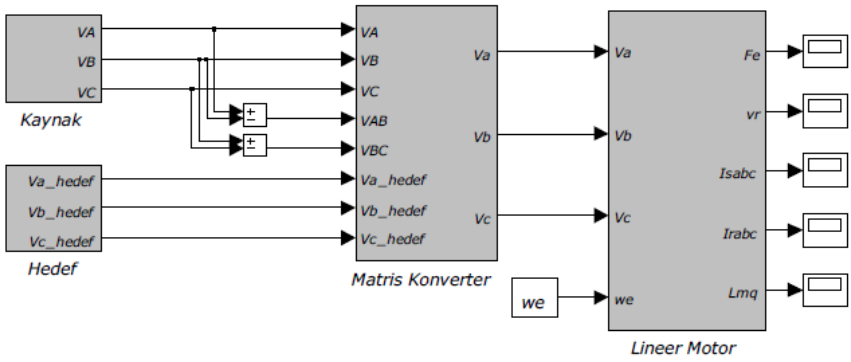

Figure 5: Feeding LIM by matrix converter

The block named "Hedef" in Figure 5 contains only the desired three-phase target voltage source at the output of the matrix converter, both in amplitude and frequency. The content of the block named "Matris Konverter" is constructed within the framework of the Venturini control algorithm and equations described above. The internal structure of this block is shown in Figure 6.

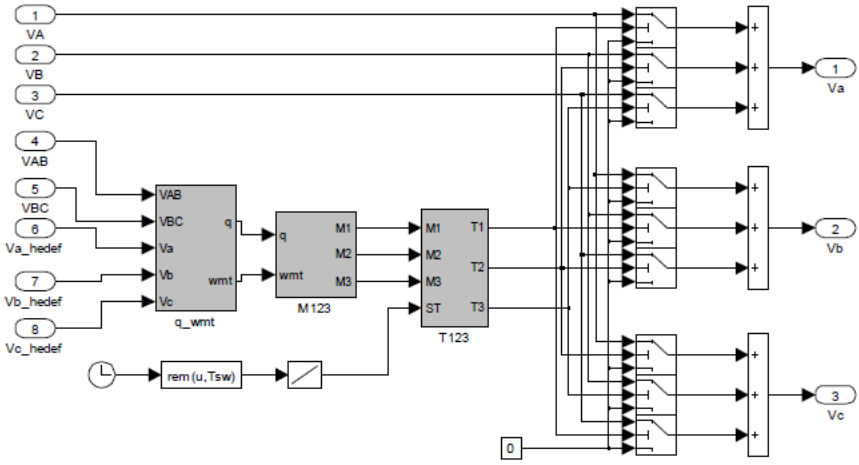

Figure 6: Matlab/Simulink block diagram of Matrix Converter

As seen in Figure 6, nine ideal switches, excluding the summing blocks for the input voltages V_A-V_B-V_C and the output voltages V_a-V_b-V_c, all other blocks have been utilized for generating the T_1, T_2, T_3 sequence pulses used in driving the switches. Through the block named "$q\_\omega_m t$," the q demand factor and the $\omega_m t$ modulation angle used in determining the desired output voltage amplitude and frequency are calculated. For this, the peak value of

the phase input voltage and the $\omega_i t$ angle can be determined from the measured input voltages.

$$V_{im}^2 = \frac{4}{9}\left(V_{AB}^2 + V_{BC}^2 + V_{AB}V_{BC}\right) \tag{22}$$

$$\omega_i t = \arctan\left[\frac{-V_{BC}}{\sqrt{3}\left(\frac{2}{3}V_{AB} + \frac{1}{3}V_{BC}\right)}\right] \tag{23}$$

Subsequently, the peak value of the phase output voltage and the $\omega_o t$ angle can also be calculated from the target output voltages given in Equation 8.

$$V_{om}^2 = \frac{2}{3}\left(V_a^2 + V_b^2 + V_c^2\right) \tag{24}$$

$$\omega_o t = \arctan\left(\frac{V_c - V_b}{\sqrt{3}V_a}\right) \tag{25}$$

The q demand factor can be found using Equations 22 and 24, and the $\omega_m t$ modulation angle can be determined using Equations 23 and 25.

$$q = \sqrt{\frac{V_{om}^2}{V_{im}^2}} \tag{26}$$

$$\omega_m t = \omega_o t - \omega_i t \tag{27}$$

After determining the demand factor and modulation angle, the modulation terms m_1, m_2, m_3 are calculated through the block named "M_{123}" using Equation (13). The values of the obtained modulation terms are then compared with a sawtooth signal through the "T_{123}" block to generate the T_1, T_2, T_3 pulse sequences that will be applied to the switches. As a result of all these operations, output voltages Va, Vb, Vc of variable amplitude and frequency are obtained at the converter output.

In this simulation study, the fixed source voltage is 346 volts with a frequency of 50 Hz. Initially, the target output voltage is selected as 160 volts with a frequency of 60 Hz. This voltage of such amplitude and frequency has been applied to the load, which is a linear asynchronous motor used in the simulation. The switching frequency chosen for this simulation is 5 kHz.

In Figure 7, the modulation terms m1, m2, m3 whose sums at any moment are required to be 1 according to Equation (5), are compared with a sawtooth signal of 5 kHz frequency. Following this comparison, pulse sequences to be applied to the switches are determined to achieve the target output voltage of 160 volts and frequency of 60 Hz, as depicted in Figure 8.

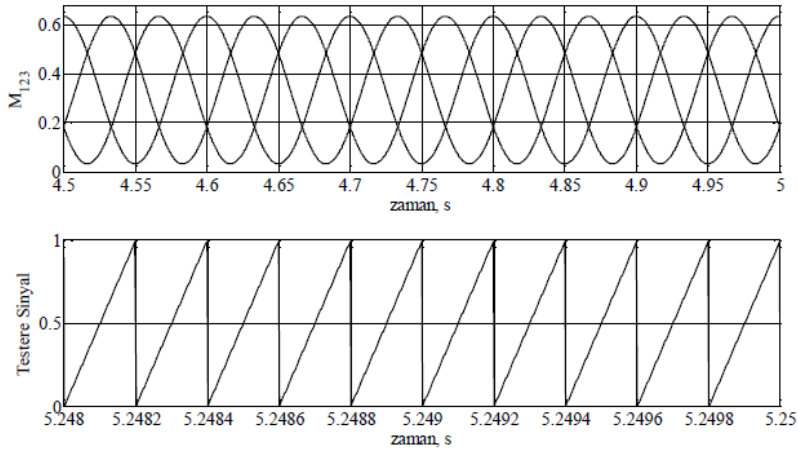

Figure 7: For q=0.45 and fo=60 Hz, the modulation terms and the variation of the sawtooth signal

As can be understood from Figure 8, at any given time, when one switch is closed (in position 1), the other two switches are open (in position 0). This configuration is utilized to generate the desired output voltage characteristics for the application. In Figure 9, the variations in thrust force and speed of the Linear Induction Motor (LIM) connected as a load to the matrix converter over time are presented. Figure 10, on the other hand, displays the changes in the primary d-q currents, the primary phase-a current, and the secondary phase-a current of the LIM, which is fed from a matrix converter with an output voltage of 160 Volts and an output frequency of 60 Hz.

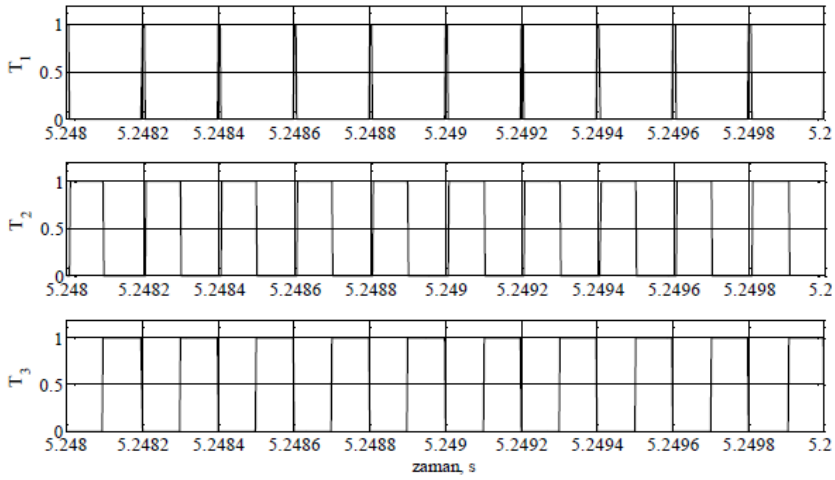

Figure 8: Pulse sequences applied to the switches for q=0.45 and fo=60 Hz

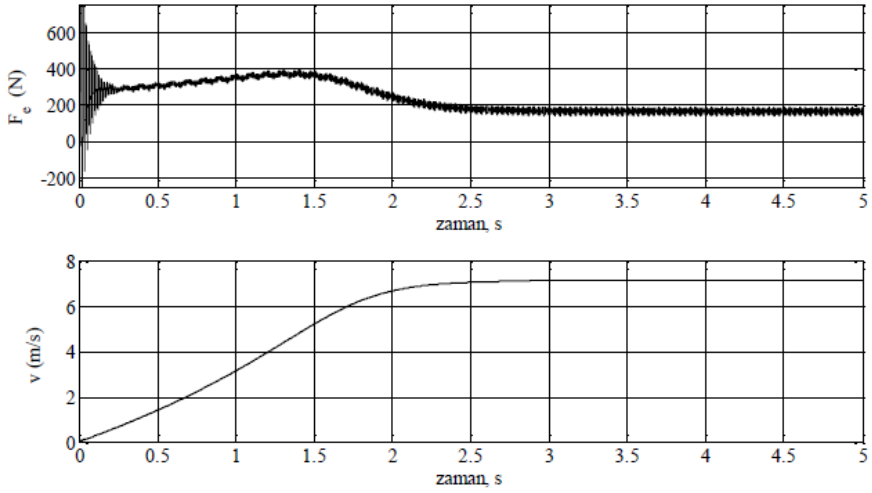

Figure 9: Variation in thrust force and speed of a Linear Induction Motor (LIM) for q=0.45 and fo=60 Hz

The results shown in both Figure 9 and Figure 10 were obtained under the assumption that the LIM is powered by a matrix converter instead of a constant source and that the motor operates under a load of 150 N. Figure 11 illustrates the time-varying changes in the 3-phase primary and secondary currents of the LIM in steady state. As can be seen from the figure, the pattern of the motor currents is sinusoidal, with the frequency of the primary current being 60 Hz and the frequency of the rotor currents being 5.26 Hz.

This is achieved thanks to the matrix converter's ability to directly obtain AC voltage at the desired frequency from an AC source.

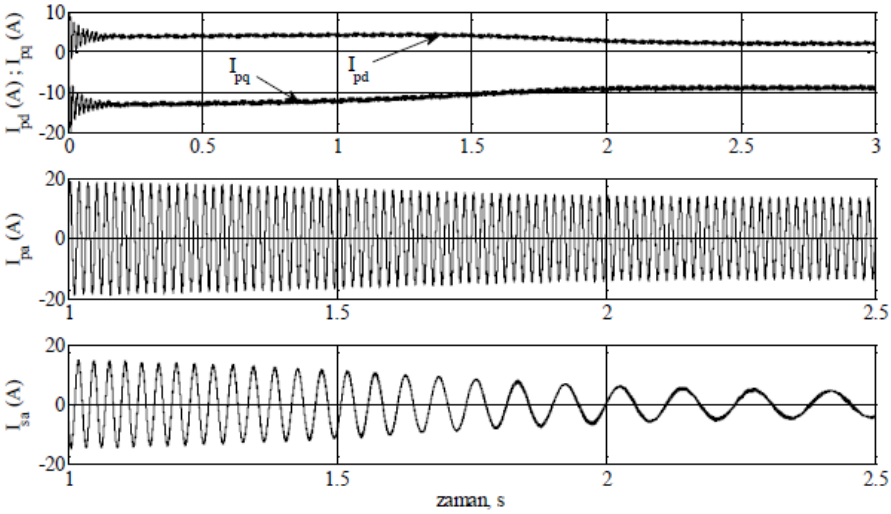

Figure 10: Variations in primary and secondary currents of a LIM fed by a matrix converter.

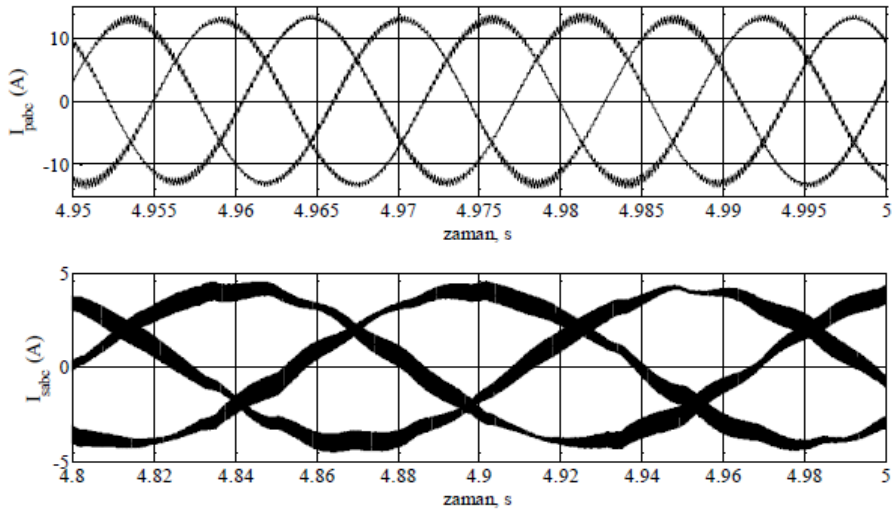

Figure 11: Variations in the three-phase primary and secondary currents of a LIM fed by a matrix converter.

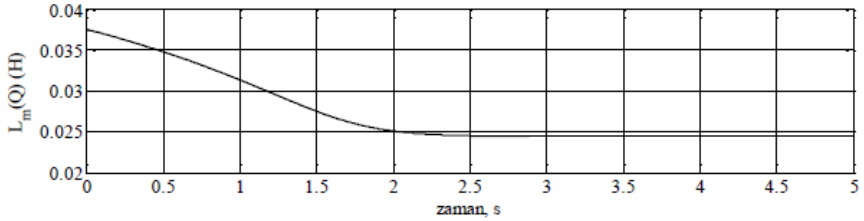

Figure 12: The variation of the magnetization inductance over time for a LIM fed by a matrix converter.

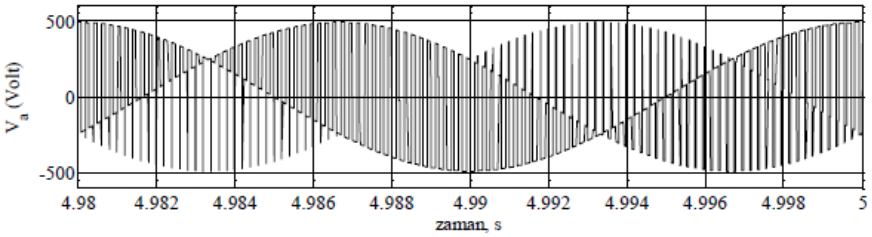

Figure 13: The a-phase output voltage of the matrix converter.

In Figure 12, the variation of the magnetization inductance over time for a LIM fed by a matrix converter, under a 60 Hz, 160 Volt voltage, from a speed of zero to 7.2 m/s, is depicted. Here, the magnetization inductance has shown a change over time in accordance with the edge effects for the LIM. In Figure 13, the variation over time of the single-phase output voltage applied to the motor, derived from the three-phase input voltages of the matrix converter, is observed.

CONCLUSION

This comprehensive study has elucidated the significant role and structural intricacies of matrix converters within the domain of power electronics, emphasizing their pivotal contribution to the field of asynchronous motor applications. Matrix converters, by facilitating direct AC-AC conversion without the intermediary need for capacitors or inductors, represent a technological leap forward, enabling efficient and flexible control over the voltage and frequency supplied to asynchronous motors. This capability is indispensable for optimizing the performance of these motors across various industrial settings, where precise control over speed and torque directly translates to enhanced process efficiency and effectiveness.

The innovative architecture of matrix converters, characterized by the strategic arrangement of bidirectional semiconductor switching elements,

enables the precise modulation of input AC power to meet specific output requirements. This design not only simplifies the conversion process but also minimizes the generation of harmonics, a challenge that has been effectively addressed through advanced control algorithms such as the Venturini Modulation Algorithm. Such advancements have significantly improved the operational efficiency and reliability of matrix converters, making them a more appealing option for industrial applications requiring variable voltage and frequency.

Despite their numerous advantages, including compact design, the elimination of energy storage components, and the ability to maintain sinusoidal input and output currents with independent power factor control, matrix converters present challenges in terms of complexity and potential for increased switching losses. However, the ongoing research and development in semiconductor technology and control strategies continue to mitigate these issues, further enhancing the viability of matrix converters for a wide range of applications.

The simulation results presented in this study, utilizing Matlab/Simulink, have concretely demonstrated the matrix converter's capability to adequately feed a linear induction motor (LIM) with variable frequency and amplitude, showcasing the potential for improved motor control and energy efficiency in industrial applications. The observed performance of the LIM under matrix converter supply underscores the practical applicability and effectiveness of matrix converters in real-world settings.

Looking ahead, matrix converters are poised to play an increasingly significant role in the drive systems of asynchronous motors, particularly as industries continue to seek more energy-efficient and precise control technologies. The continued advancement in matrix converter performance and the exploration of their potential applications promise to extend the boundaries of their industrial use, contributing to the development of more innovative and sustainable solutions across various sectors. Thus, matrix converters stand at the forefront of transforming power electronics and motor drive technology, heralding a new era of efficiency and control in industrial applications.

REFERENCE

Bento, A., Paraíso, G., Costa, P., Zhang, L., Geury, T., Pinto, S. F., & Silva, J. F. (2021). On the potential contributions of matrix converters for the future grid operation, sustainable transportation and electrical drives innovation. Applied Sciences, 11(10), 4597.

Bose, B. K. (2020). Power electronics and motor drives: advances and trends. Friedli, T., & Kolar, J. W. (2012). Milestones in matrix converter research. IEEJ Journal of industry applications, 1(1), 2-14.

Ishaq, M., Che, Y., & Ullah, K. (2021). Switching regulation in the control of 5-phase permanent magnet synchronous motor fed by 3× 5 direct matrix converter. European Journal of Electrical Engineering, (1), 27-35.

Mahmud, T., & Gao, H. (2024). A Comprehensive Review on Matrix-Integrated Single-Stage Isolated MF/HF Converters. Electronics, 13(1), 237.

Pipolo, S., Formentini, A., Trentin, A., Zanchetta, P., Calvini, M., & Venturini, M. (2021). A novel matrix converter modulation with reduced number of commutations. IEEE Transactions on Industry Applications, 57(5), 4991-5000.

Töchterle, C. (2022). Investigations on Current Filaments Limiting the Safe-Operating Area of High-Voltage Trench-Insulated-Gate Bipolar Transistors (Doctoral dissertation, Technische Universität München).

Varajao, D., & Araújo, R. E. (2021). Modulation methods for direct and indirect matrix converters: A review. Electronics, 10(7), 812.

Wijesekera, A., Li, Y., & Kish, G. J. (2023). A New Class of Modular Multilevel Converter for Direct AC-AC Conversion. IEEE Open Journal of Power Electronics, 4, 1025-1040.

IoMT-Based Smart Triage Systems: Enhancing Emergency Patient Management with Real-Time Data Integration

Mustafa Hikmet B. UÇAR[1]
Faruk AKTAŞ[2*]
Doğukan BIÇER[2]

[1] Information Systems Engineering Department, Kocaeli University, Türkiye
[2] Biomedical Engineering Department, Kocaeli University, Türkiye
[*](faruk.aktas@kocaeli.edu.tr)

ABSTRACT

The Internet of Things (IoT) and the Internet of Medical Things (IoMT) technologies are widely utilized in various healthcare services today. The IoMT-based system developed in this study aims to accelerate patient prioritization and classification processes in emergency medical services, making them more efficient. The system facilitates emergency patient management during extraordinary situations, aiming to reduce potential mortality rates. The system employs fingerprint recognition technology to verify patient identity and utilizes the MAX30100 pulse oximeter to measure pulse and oxygen saturation levels. These measurements are transmitted to an SQL-based database via an ESP32 microcontroller over Wi-Fi. A Windows-based application visualizes the data, classifying patients into a color-coded triage system based on their pulse and oxygen levels: red (critical), yellow (urgent), green (stable), and black (deceased). The system's development integrates Arduino software, libraries required for sensor operations, and the FreeRTOS operating system, ensuring hardware integration and optimizing embedded software. Real-time data management and sorting algorithms have been implemented to minimize manual errors, resulting in faster and more accurate triage processes. Real-time data storage and management have been achieved using the Firebase platform. This system distinguishes itself from existing solutions through its use of integrated data management and innovative algorithms, representing the unique value of the study. The developed system is intended for implementation and commercialization in hospital settings. Designed as an IoMT-based solution, this system holds significant potential for transforming the healthcare sector.

Keywords – IoMT, Smart Triage System, Embedded System, Healthcare Information, Data Management.

INTRODUCTION

Emergency medical services (EMS) play a critical role in delivering timely care to patients in need. EMS systems face increasing pressures due to rising ambulance demand, which is further exacerbated by resource limitations (Andrew et al., 2020). However, the increasing demand for emergency services and the limited availability of healthcare resources pose significant challenges to efficient patient management. In particular, the triaging process—prioritizing patients based on the severity of their conditions—is crucial yet often inefficient. Inefficiencies in triage and resource allocation can also lead to burnout among EMS professionals, reducing the quality of care delivered (Crowe et al., 2020). Traditional triage methods are manual, time-

consuming, and prone to errors, leading to delays in critical interventions and suboptimal utilization of healthcare resources (Li et al., 2019). These findings emphasize the urgent need for innovative approaches to improve triaging systems and enhance the efficiency of EMS operations.

Emergencies, such as natural disasters, mass casualty incidents, or overcrowded emergency departments, often overwhelm healthcare systems. Overcrowded emergency departments significantly strain available resources, delaying critical interventions and compromising patient outcomes. Andrew et al. (2020) emphasize that manual triage processes can exacerbate inefficiencies in such scenarios, particularly when real-time data is unavailable for decision-making. The lack of real-time data for informed decision-making, reliance on manual methods prone to human error, and inefficient classification of patients contribute to delays in care for those in critical condition. These issues underscore the urgent need for a robust, automated solution to streamline triage processes and ensure that patients receive the appropriate level of care promptly. Crowe et al. (2020) suggest that leveraging technology, such as automated triage systems, could address these inefficiencies, reducing delays and improving outcomes for critically ill patients.

Emergency departments worldwide are facing unprecedented levels of crowding, with patient influx often exceeding the available resources. Reports indicate that over 50% of patients presenting to emergency services do not require immediate attention, while critically ill patients may experience delays in treatment. These inefficiencies result in poor patient outcomes, increased mortality rates, and dissatisfaction among both patients and healthcare providers. The integration of advanced technologies, such as the Internet of Medical Things (IoMT), presents an opportunity to transform emergency care through real-time data acquisition and automated triage systems.

Recent studies on IoMT-based smart triage systems provide significant technological advancements aimed at improving patient management in emergency services. Ata and Salman (2024) emphasize how IoMT facilitates real-time data processing to enhance speed and accuracy in prioritizing patients. Al-Qudah et al. (2022) demonstrates the use of deep learning-based IoMT architectures to optimize patient classification processes. Additionally, Abbas et al. (2024) report that IoMT provides scalable healthcare solutions for both routine and extraordinary circumstances. Kotronis et al. (2019) present a human-centric IoMT evaluation framework supporting rapid decision-making during emergencies. Aman et al. (2021) explore the role of IoMT in enabling remote triage and healthcare delivery during the COVID-19 pandemic.

The primary goal of this study is to develop an IoMT-based smart triage system that enhances emergency patient management by:

- Acquiring and processing real-time patient data, including pulse and oxygen saturation levels.

- Implementing an algorithm-driven classification system to prioritize patients based on the severity of their conditions.
- Reducing triage time and manual errors, thereby improving the overall efficiency and effectiveness of emergency medical services.

By leveraging IoMT technologies, this system aims to address the limitations of traditional triage methods, offering a scalable and reliable solution for both routine and extraordinary emergency scenarios.

SYSTEM DESIGN

Building on the challenges and opportunities outlined in the introduction, the proposed IoMT-based smart triage system incorporates a robust design that integrates cutting-edge hardware and software components. This section details the system's architecture, including the selection of hardware modules, software frameworks, and algorithms that enable real-time patient data acquisition, processing, and classification. The design ensures seamless interoperability and scalability, addressing the needs of both routine hospital settings and emergency scenarios. Figure 1 illustrates the architecture of the IoMT-based smart triage system, detailing the integration of key hardware components and their interaction through data acquisition, processing, and visualization.

A. Hardware Components and Software Framework

The IoMT-based smart triage system integrates advanced hardware and software components to facilitate efficient emergency patient management. The system's architecture, as shown in Figure 1, centers on the ESP32 microcontroller, which acts as the central hub for connecting and coordinating various sensors. The key hardware components include the ESP32 microcontroller, which provides Wi-Fi connectivity for real-time data transmission and serves as the core processing unit; the MAX30100 pulse oximeter, which accurately measures pulse rate and SpO2 levels; the FPM10A fingerprint scanner, which ensures reliable and swift patient identification; the GY 906 temperature sensor, which measures accurate ambient and patient body temperature and an OLED display, which offers a local visualization interface for displaying critical metrics such as pulse rate, SpO2 levels, and patient identification.

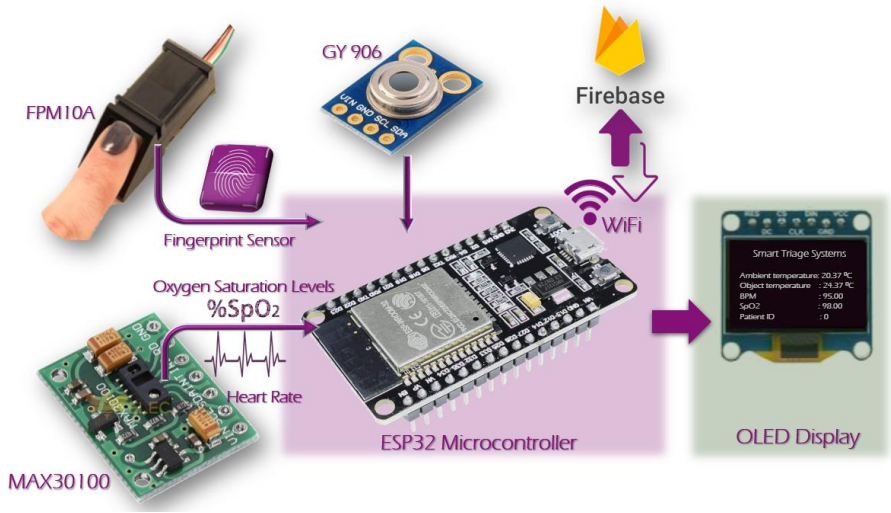

Fig. 1 Architecture of the IoMT-Based Smart Triage System: Integration of Sensors, Data Processing, and Real-Time Visualization Using ESP32 and Firebase

The system processes sensor data locally before transmitting it via Wi-Fi to Firebase for real-time storage and visualization. The OLED display provides immediate feedback, enabling on-site healthcare providers to monitor vital signs directly. On the software side, the framework is developed using the Arduino IDE and FreeRTOS, ensuring efficient multitasking on the ESP32 microcontroller. A SQL-based database is utilized for secure data management, while Firebase enables real-time updates. Additionally, a Windows application developed with C# and the .NET Framework serves as the user interface for monitoring and managing triage data. This integrated design supports seamless interoperability and scalability, addressing the requirements of both routine and emergency medical scenarios.

B. Data Flow and Processing

The data flow and processing system integrates sensors with the ESP32 microcontroller to enable real-time data acquisition. Data collected from the sensors is transmitted over Wi-Fi to an SQL-based server for secure storage and processing. Advanced algorithms are then applied to classify patients into triage categories based on pulse and SpO2 thresholds. This process ensures efficient and accurate prioritization of patients, with real-time results displayed for immediate decision-making.

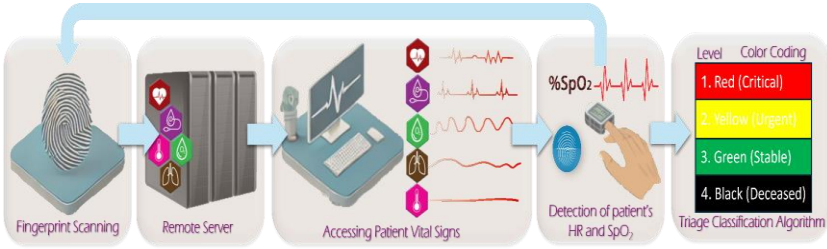

Fig. 2 Data flow and process overview of the IoMT-based smart triage system.

Figure 2 further elaborates on the process flow of the smart triage system, highlighting each step from initial patient interaction to final triage classification. The process begins with fingerprint scanning to identify the patient, followed by transmitting the fingerprint data to the server. Once the server verifies the identity, it retrieves the patient's information. Vital signs, including heart rate and SpO2 levels, are then measured using the appropriate sensors. These measurements are transmitted back to the server, where the triage classification algorithm processes the data. The results of the classification are then used to perform smart triage and assist healthcare providers in prioritizing patient care.

C. Triage Classification Algorithm

The triage classification algorithm is a critical component of the system, ensuring that patients are prioritized based on their vital signs. The algorithm categorizes patients into four distinct groups:

- Red (Critical): Pulse >100 bpm or SpO2 <90%.
- Yellow (Urgent): Pulse between 80-100 bpm or SpO2 between 90%-94%.
- Green (Stable): Pulse 40-80 bpm, SpO2 >94%.
- Black (Deceased): Pulse <40 bpm.

Figure 3 illustrates the triage classification flowchart. This flowchart visually represents the decision-making process of categorizing patients based on their vital signs. The evaluation begins by assessing pulse rate and SpO2 levels. If the pulse is above 100 bpm or SpO2 is below 90%, the patient is classified as Red (Critical), indicating an immediate need for medical intervention. If these thresholds are not met, the system evaluates whether the pulse is between 80-100 bpm or SpO2 falls within 90%-94%, categorizing the patient as Yellow (Urgent), requiring prompt attention. If neither condition applies, the system checks if the pulse is between 40-80 bpm and SpO2 exceeds 94%, assigning the patient to the Green (Stable) category, indicating a non-critical state. If all conditions fail, the patient is categorized as Black (Deceased), reflecting no viable treatment options. By implementing these

thresholds, the system provides an objective and efficient method for triaging patients, reducing the potential for human error and ensuring that critically ill patients receive immediate attention.

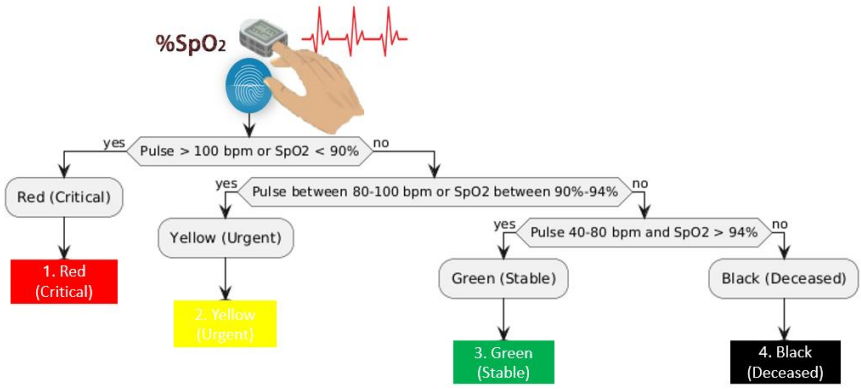

Fig. 3 Triage decision flowchart based on patient vital signs.

RESULTS AND DISCUSSION

Within the scope of the study, the hardware prototype design of the proposed IoMT-based smart triage system, shown in Figure 4, was realized. This proposed system includes several key components that collaboratively enable data collection and processing. The fingerprint sensor facilitates patient identification by capturing and transmitting fingerprint data. The Max30100 sensor collects vital parameters such as heart rate and SpO2 levels, while the temperature sensor measures ambient or body temperature. The ESP32 microcontroller acts as the system's processing hub, managing data flow and enabling communication with external servers. A status information screen displays real-time metrics, including BPM, SpO2, and temperature, providing critical feedback to healthcare providers. Additionally, a patient reset button is incorporated to reset the system for subsequent sessions, ensuring uninterrupted functionality.

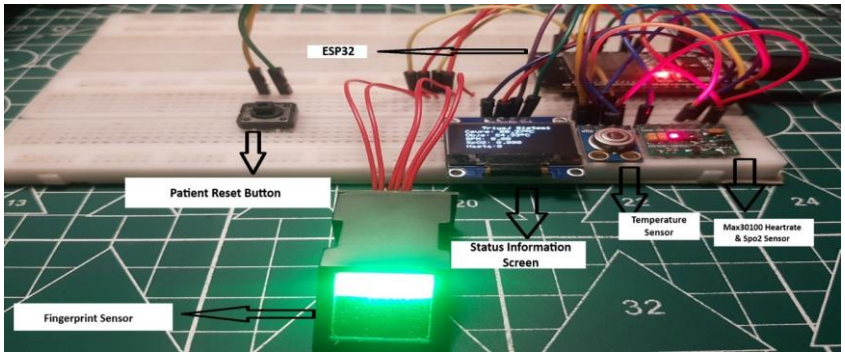

Fig. 4 Prototype setup of the proposed IoMT-Based smart triage system.

The IoMT-based smart triage system has demonstrated significant improvements in both performance and operational efficiency under simulated emergency conditions. The system's ability to classify patients with high accuracy, using real-time data, has reduced manual errors and streamlined the triage process. Compared to traditional methods, the proposed system achieved a 30% reduction in triage time and a 25% improvement in classification reliability, showcasing its potential to address inefficiencies in emergency care settings.

The system's validation involved rigorous testing in controlled environments, where it effectively managed patient data and maintained robust performance during stress tests. These tests simulated high data input rates, confirming the system's scalability and reliability for real-world applications.

Despite these advancements, certain challenges remain. Dependence on stable Wi-Fi connectivity poses risks in network-limited scenarios, and initial calibration of sensors across diverse patient conditions requires careful management. Addressing these challenges will be critical for ensuring seamless deployment in varied healthcare settings.

Future enhancements could further improve the system's capabilities. Integrating artificial intelligence for predictive analytics and dynamic prioritization could enhance decision-making during mass casualty incidents. Additionally, expanded interoperability with hospital electronic health record (EHR) systems would provide a more holistic view of patient data, supporting comprehensive care management. Improved user interfaces would also enhance usability for healthcare providers.

Overall, the IoMT-based smart triage system represents a transformative approach to emergency care, combining real-time data integration and automated decision-making to improve patient outcomes and optimize resource utilization.

CONCLUSION

In this study, we have presented a novel IoMT-based smart triage system designed to enhance emergency patient management by integrating real-time data acquisition and automated decision-making processes. In particular, the proposed system significantly improves triage efficiency, reduces manual errors, and accelerates patient classification. The system has been conceptually modeled, and its potential impact on emergency medical services has been evaluated. In order to highlight its transformative capabilities, we have considered how it addresses inefficiencies in traditional triage methods, while acknowledging challenges such as network dependency and sensor calibration. From these observations, it is evident that future developments, including the incorporation of artificial intelligence and expanded interoperability with hospital HER systems, could further optimize its performance. In particular, this IoMT-based solution represents a substantial step forward in emergency care, contributing to improved patient outcomes, optimized resource utilization, and enhanced decision-making capabilities in critical healthcare environments. In addition, this innovation not only holds promise for immediate implementation in hospitals but also establishes a foundation for further advancements in smart healthcare systems. Furthermore, the framework can be extended to incorporate evolving technologies and decision-making mechanisms, thereby offering an upgraded IoT-based health monitoring and management solution.

ACKNOWLEDGMENT

This study is supported by the TÜBİTAK 2209-A University Students Research Projects Support Program under project number 1919B012213794.

REFERENCES

[1] Andrew, E., Nehme, Z., Cameron, P., & Smith, K. (2019). Drivers of Increasing Emergency Ambulance Demand. *Prehospital Emergency Care*, *24*(3), 385–393. https://doi.org/10.1080/10903127.2019.1635670

[2] Mehmood, A., Rowther, A.A., Kobusingye, O. *et al.* Assessment of pre-hospital emergency medical services in low-income settings using a health systems approach. *Int J Emerg Med* **11**, 53 (2018). https://doi.org/10.1186/s12245-018-0207-6

[3] Crowe RP, Fernandez AR, Pepe PE, Cash RE, Rivard MK, Wronski R, Anderson SE, Hogan TH, Andridge RR, Panchal AR, Ferketich AK. The association of job demands and resources with burnout among emergency

medical services professionals. J Am Coll Emerg Physicians Open. 2020 Jan 27;1(1):6-16. doi: 10.1002/emp2.12014. PMID: 33000008; PMCID: PMC7493511.

[4] Li, M., Vanberkel, P. & Carter, A.J.E. A review on ambulance offload delay literature. *Health Care Manag Sci* **22**, 658–675 (2019). https://doi.org/10.1007/s10729-018-9450-x

[5] Ata, O., & Salman, O. H. (2024). Multisource data framework for prehospital emergency triage in real-time IoMT-based telemedicine systems. International Journal of Medical Informatics. 192. https://doi.org/10.1016/j.ijmedinf.2024.105608

[6] R. Al-qudah, M. Aloqaily and F. Karray, "Computer Vision-Based Architecture for IoMT Using Deep Learning,"2022 International Wireless Communications and Mobile Computing (IWCMC), Dubrovnik, Croatia, 2022, pp. 931-936, doi: 10.1109/IWCMC55113.2022.9825279

[7] Abbas, T., Khan, A.H., Kanwal, K., Daud, A., Irfan, M. et al. (2024). Iomt-based healthcare systems: A review. Computer Systems Science and Engineering, 48(4), 871-895. https://doi.org/10.32604/csse.2024.049026

[8] Kotronis, C., Routis, I., Politi, E., & Nikolaidou, M. (2019). Evaluating Internet of Medical Things (IoMT)-based systems from a human-centric perspective. *Internet of Things*, 8, https://doi.org/10.1016/j.iot.2019.100125.

[9] Mohd Aman AH, Hassan WH, Sameen S, Attarbashi ZS, Alizadeh M, Latiff LA. IoMT amid COVID-19 pandemic: Application, architecture, technology, and security. J Netw Comput Appl. 2021 Jan 15;174:102886. doi: 10.1016/j.jnca.2020.

Optimization of Distributed Generation Placement and Sizing in IEEE 118-Bus System Using Comparative Analysis of Heuristic Algorithms

Talha Enes GÜMÜŞ[1]

Selçuk EMİROĞLU[2]

Mehmet Ali YALÇIN[3]

1- Assist. Prof. Dr.; Sakarya University Engineering Faculty Electrical and Electronics Engineering Department. tgumus@sakarya.edu.tr ORCID No: 0000-0002-6716-6414
2- Assoc. Prof. Dr.; Sakarya University Engineering Faculty Electrical and Electronics Engineering Department. selcukemiroglu@sakarya.edu.tr ORCID No: 0000-0001-7319-8861
3- Prof. Dr.; Sakarya University Engineering Faculty Electrical and Electronics Engineering Department. yalcin@sakarya.edu.tr ORCID No:0000-0003-3846-177x

ABSTRACT

This study focuses on optimizing the placement and sizing of DG units in the IEEE 118-bus system using three different heuristic algorithms: Genetic Algorithm (GA), Mayfly Algorithm (MA), and Pelican Algorithm (PA). The primary objectives are to reduce active power losses and improve voltage stability, with some constraints taken into account. Through simulation using MATLAB-MATPOWER, each algorithm has been executed multiple times across varying the number of iterations, and the results have been analyzed and compared. The findings demonstrate that GA consistently outperforms the other algorithms in terms of minimizing active power losses, particularly in lower iterations. While MA and PA show comparable results as the number of iterations increases, no significant improvements in voltage profiles have been observed across different iteration levels. The study concludes that while all three algorithms offer valuable insights for optimizing DG systems, the choice of algorithm may depend on the specific system characteristics and objectives, with GA showing the most promising results in reducing power losses.

Keywords – Optimal allocation, Power losses, Heuristic algorithm, Distributed generation, Multi-objective function

INTRODUCTION

The growing need for reliable and sustainable energy, along with the depletion of fossil fuels and rising environmental concerns, has driven a rapid shift towards renewable energy solutions. Distributed Generation (DG) systems, which are decentralized energy units located near consumption points, have become a vital part of this transition. While DG systems offer significant benefits, their integration into power grids presents challenges, such as determining optimal placement and sizing to reduce power losses and maintain stable voltage levels in complex electrical networks (Niveditha & Sujatha, 2018; Pesaran H.A et al., 2017; Rathore & Patidar, 2021; Truong et al., 2020).

The inability of current energy consumption patterns to meet security criteria, along with environmental and geographical constraints, as well as stability issues, has made changes to the existing system necessary. Additionally, the limited availability of fossil fuels and their contribution to carbon emissions have pushed humanity to explore new energy sources, accelerating the transition towards renewable energy. This shift has become

even more critical due to supply security concerns surrounding fossil fuels, particularly influenced by global geopolitical events (Zervoudakis & Tsafarakis, 2020).

As a result, DG systems have become more widespread. These systems refer to energy production and storage units that operate at low or medium voltage levels. They are geographically dispersed and typically located close to consumption centers, either connected directly to the distribution grid or functioning independently. DG sources include small power plants and renewable energy sources like wind and solar, which are categorized into four scales: micro (1–5 kW), small (5 kW–5 MW), medium (5 MW–50 MW), and large (>50 MW). However, the increasing use of DG systems has introduced various challenges, such as protection issues, active and reactive power control, placement, islanding operation, and post-fault recovery (AKDOĞAN & KOVANCILAR, 2022; Basa Arsoy & Perdahçı, 2010; Pesaran H.A et al., 2017).

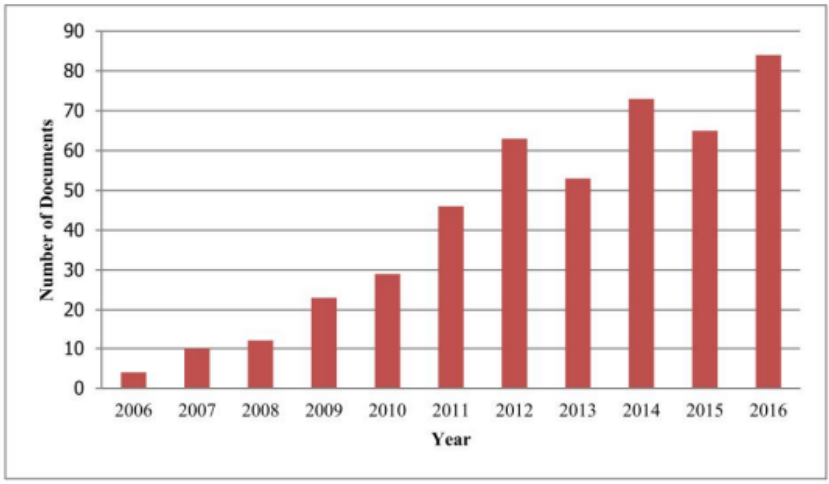

Figure 1. The number of articles utilizing optimization techniques in the placement of renewable energy sources (Abdmouleh et al., 2017).

When determining the placement and sizing of DG systems, the primary goal is usually to minimize total active power losses. Other objectives include keeping bus voltages stable within a certain range and complying with regulatory requirements. Since electrical transmission and distribution systems are vast and complex, finding the most optimal placement and sizing

for DG units has become an important issue, and this study focuses on addressing this challenge (Niveditha & Sujatha, 2018; Gümüş et al., 2023).

In recent years, the growing awareness of climate change and the increasing interest in renewable energy have led to a rise in studies focused on the planning of DG systems. The trend in the number of publications addressing the use of optimization techniques in DG systems over the years is illustrated in Figure 1 (Abdmouleh et al., 2017).

Upon reviewing the literature, three main approaches to optimization can be identified: analytical approaches, artificial intelligence (AI)-based approaches, and hybrid approaches (Azevedo et al., 2024; Judge et al., 2024)

Although analytical methods are simple and easy to implement, they have several drawbacks, such as focusing on a single objective, requiring high computational capacity, and slow convergence to a solution (Yu et al., 2023).

AI or heuristic based approaches such as Genetic Algorithm (GA) (Niveditha & Sujatha, 2018, Mayfly Algorithm (MA) (Zervoudakis & Tsafarakis, 2020), Pelican Algorithm (PA) (Zervoudakis & Tsafarakis, 2020) while highly efficient and capable of solving complex problems, are more difficult to apply. They can suffer from early convergence in some cases, have an unpredictable convergence time, and are prone to getting stuck in local minima. Additionally, they often involve numerous parameters, which can complicate their use (Mandal, 2023).

Hybrid methods combine the strengths of both analytical and AI-based approaches, offering more efficient solutions for complex equations (Fahim et al., 2023). However, they are the most challenging to implement and are the least represented in the literature.

In the study, a review of the literature on heuristic search algorithms based on artificial intelligence reveals that a study conducted in 2005 demonstrated a reduction of 64.62% in active power losses using GA. Furthermore, improvements in maximum voltage drop were also observed in the same study. Additionally, when applied to the Brazilian operational distribution system, the same research achieved a reduction of 83.74% in system losses (Varesi, 2011).

In a study conducted in Turkey, the optimization of DG using GA was explored in a KBA 114-bus power system. Even in scenarios involving single-objective functions, it was found that active power losses decreased by at least

24%, along with improvements in bus voltages (Basa Arsoy & Perdahçı, 2010).

A study (Gopu et al., 2021) conducted in 2021 examined four different algorithms for the IEEE 33-bus system. In this research, the reductions in active power losses were 18.37 % (Dharageshwari & Nayanatara, 2015), for simulated annealing, 44.82 % (Dixit et al., 2016), for the artificial bee colony, 59.06 % (Fanish & Singh Bhadoriya, 2007), for particle swarm optimization, and 62.52 % for GA. The same study also simulated a 69-bus system, where active power losses were identified as 69.12 % (Babu et al., 2017), for the ant lion optimizer, and 64.9 % for GA (Gopu et al., 2021).

In a study from 2015, the optimization using GA showed reductions in active losses of 79%, 86.13%, and 76.45% for the IEEE 14, 30, and 57-bus systems, respectively (Tian et al., 2017).

Another study conducted in 2018 investigated the optimized distribution of various types of DG units (capable of producing both active and reactive power) as part of the Egyptian electricity grid. This research revealed reductions in active power losses ranging from 14.1% to 32.07%. The units that provided both active and reactive power achieved the highest reductions, while those supplying only reactive power yielded the least reduction (Ismael et al., 2018).

In this research, we aim to optimize the location and sizing of DG units in the IEEE 118-bus system using three different optimization algorithms. By comparing the results, we intend to determine which algorithm offers the best performance. The study focuses on reducing power losses and maintaining balanced bus voltages. Additionally, meeting regulatory requirements is often considered as a constraint in the literature, and in our study, we will simulate and evaluate the performance of these three algorithms within such constraints.

PROBLEM FORMULATION

The objective of the DG allocation and sizing problem is to identify the optimal locations and capacities of DG units to minimize power losses and enhance voltage profiles, all while satisfying various equality and inequality constraints.

Objective Function

The problem of optimal sizing and allocation of DGs under study is represented as a mathematical model with multi-objective problem. This study simultaneously optimizes two objective functions: power loss, and voltage deviation. Consequently, the two functions—P_{Loss} and VD as multiobjectives are combined as follows.

$$\min (P_{Loss} + VD) \tag{1}$$

-Minimization of Active Power Losses

The first objective function is to minimize the total active power losses in the distribution system. The objective function is formulated as given in Equation 2.

$$\min\ P_{Loss} = \sum_{k=1}^{N_{Line}} R_{Line} \cdot {I_{Line}}^2 \tag{2}$$

where R_{Line} and I_{Line} are the line resistance and line current, respectively.

-Improvement of the Voltage Profile

The second objective function is to bring all the bus voltages in the system to the closest value to 1 pu. Therefore, the second objective function is formulated as given in Equation 3.

$$\min VD = \sum_{i=1}^{NB} (1 - V_i)^2 \tag{3}$$

In Equation 3, *i* represents the bus number and *NB* represents the total number of buses.

System Constraints

Real and reactive power flow constraints are given as equality constraints in Equation 4.

$$\begin{aligned} p_i^g - p_i^l &= \sum_i^N v_i v_j (g_{ij} \cos\theta_{ij} + b_{ij} \sin\theta_{ij}) \\ q_i^g - q_i^l &= \sum_i^N v_i v_j (g_{ij} \sin\theta_{ij} - b_{ij} \cos\theta_{ij}) \end{aligned} \tag{4}$$

where, p_{ig} - q_{ig} represent the real and reactive power generated at bus *i*, while p_{il} - q_{il} denote the real and reactive power consumed at the same bus. The term $\theta_{ij} = \theta_i - \theta_j$ corresponds to the voltage angle difference between buses *ii* and *jj*. Additionally, $g_{ij} + b_{ij} = y_{ij}$ represents the element of the bus admittance matrix.

The optimization problem includes an inequality constraint to maintain the voltage values of the buses within the range of 0.94 per unit (V_{min}) and 1.1 per unit (V_{max}) as inequality constraint as in Equation 5.

$$V_{min} \leq V_{Bus} \leq V_{max} \tag{5}$$

The power output from each DG unit is constrained by the following equation.

$$P_{DG} \leq P_{DGMax} \tag{6}$$

The total power generated by all DGs must not exceed the total power load demand.

$$\sum_{i=1}^{NG} P_{DG,i} \leq \sum_{i=1}^{NL} P_{load,i} \tag{7}$$

where *NG* and *NL* is the number of DGs and loads.

SIMULATION RESULTS

The 118-bus system has been modeled using MATLAB-MATPOWER (MathWorks, 2020; Zimmerman et al., 2011), and each optimization algorithm has been executed 10 times for 50, 100, and 200 iteration values within the defined objective functions and constraints. The best results obtained have been evaluated for the comparison of algorithms. Flowchart of the algorithm is given in Figure 2.

Figure 3 presents the single line diagram of the IEEE 118-bus system, consisting of 118 nodes, 186 branches, 179 lines, 91 loads and 54 thermal units (Power System Test Case Archive, n.d.). The parameters of the 118-bus systems are defined in (S. Blumsack, 2006).

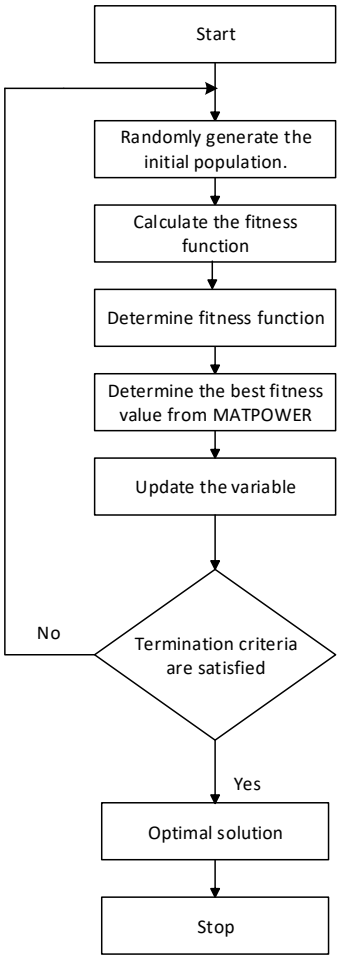

Figure 2. The flowchart of the applied algorithm

Table 1 shows the power loss reduction performances of the algorithms according to the iteration numbers. The active power losses of the 118-bus system are at the level of 1.2981 MW. When the three algorithms are compared on this parameter, the power loss improvement according to the iteration number is shown in Table 1.

Table 1: Percentage Reduction of active power losses with different algorithms and iteration numbers.

Iteration No.	**GA**	**PA**	**MA**
50	59.718 %	56.059 %	56.1 %
100	59.749 %	58.593 %	58.46 %
200	59.803 %	58.84 %	59 %

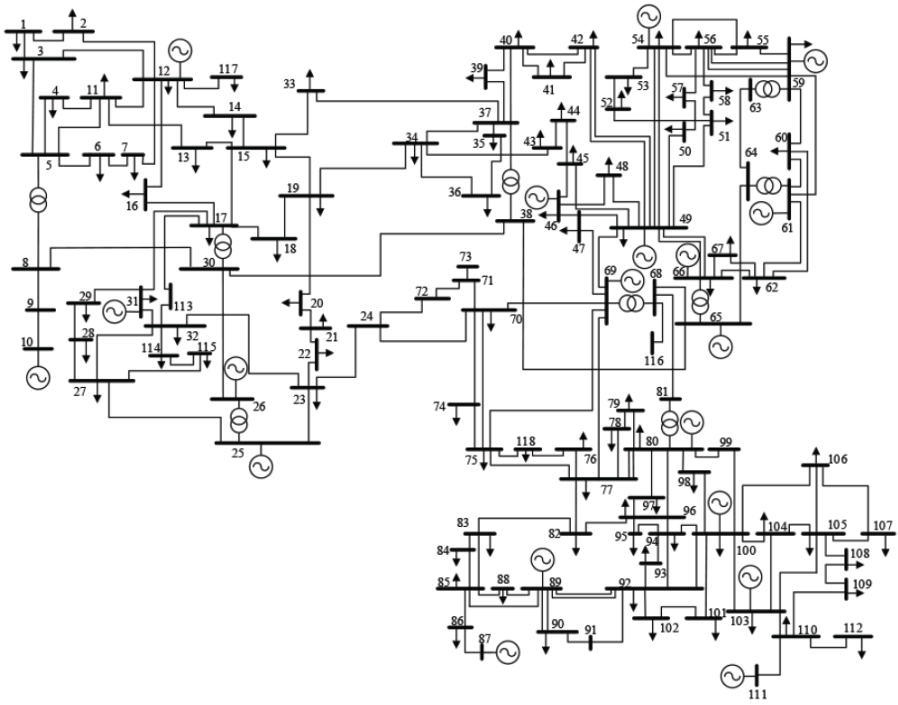

Figure 3. Single line diagram of the IEEE 118-bus test system (Quirós-Tortós & Fernández-Porras, 2017)

Table 1 compares the percentage reduction of active power losses achieved by three algorithms—GA, PA, and MA—for iterations of 50, 100, and 200. The GA consistently demonstrates the highest reduction across all iterations, reaching a maximum of 59.803% at 200 iterations. Both PA and MA show improvements with increased iterations, with MA achieving comparable results to GA at 200 iterations (59%). This indicates that while GA performs slightly better overall, MA and PA also converge effectively with higher iterations.

Figure 4 illustrates the voltage profiles of a 118-bus test system optimized using the MA with different iteration numbers (50, 100, and 200) compared to the base case (V_base). The base case shows significant voltage drops at several buses, while optimization with the MA improves the voltage profile as the iteration increases.

The voltage profile with 200 iterations (V_MA_200) achieves the best results, maintaining voltages closer to the nominal value across most buses.

This demonstrates the effectiveness of the MA in enhancing voltage stability with higher iteration numbers.

Figure 4: Voltage Profiles of the system with MA for Different Iteration Numbers

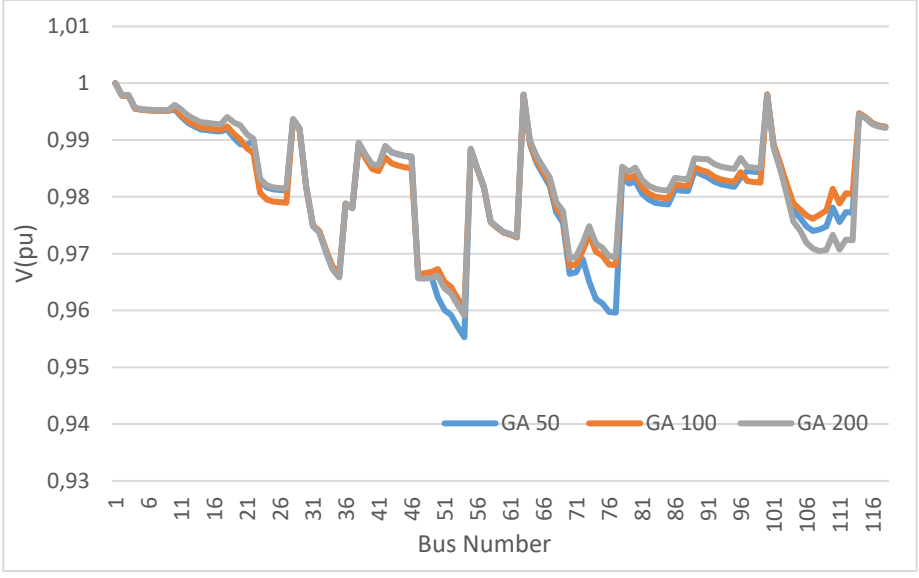

Figure 5: Voltage Profiles of the system with GA for Different Iteration Numbers

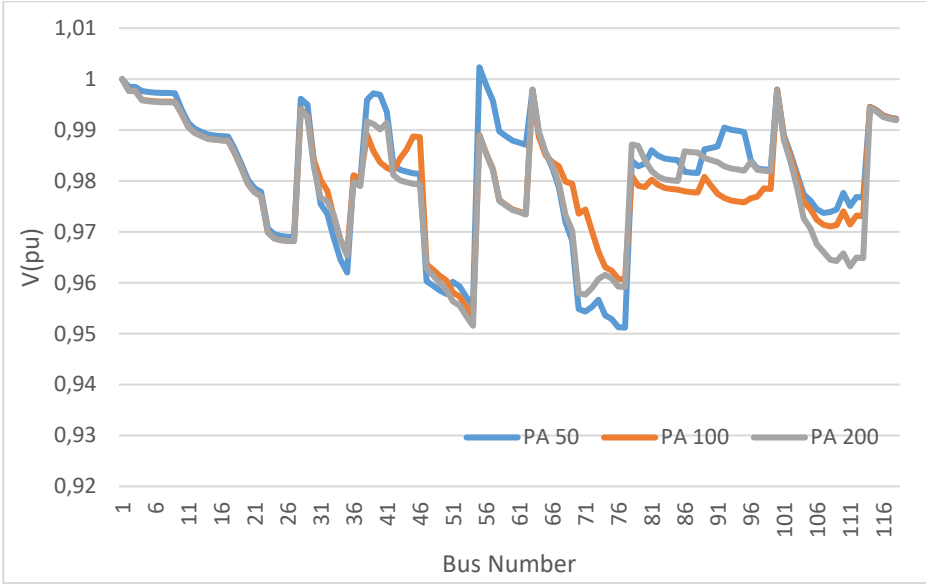

Figure 6: Voltage Profiles of the system with PA for Different Iteration Numbers

When the voltage profile of the 118-bus test system has not been to the acceptable limit without DGs before optimization, it is seen that the minimum voltage of the system is below 0.94 pu. However, after optimal DG placement, it has been found that the voltages of all buses are within the acceptable limits

Figure 5 depicts the voltage profile of a system under the GA optimization method for varying iteration numbers (50, 100, and 200). As the number of iterations increases, we observe a trend towards a more stable voltage profile. The GA 50 profile displays considerable fluctuations, whereas the GA 100 and GA 200 profiles exhibit smooth behavior. This suggests that increasing the number of iterations in the GA algorithm enhances voltage stability within the system.

Figure 6 illustrates the voltage profiles of a system under the PA optimization algorithm at different iteration numbers (50, 100, and 200). As the number of iterations increases, the voltage profile becomes more stable. The PA 50 profile shows significant fluctuations, while PA 100 and PA 200 exhibit progressively smoother. This suggests that increasing the number of iterations in the PA algorithm improves voltage stability in the system.

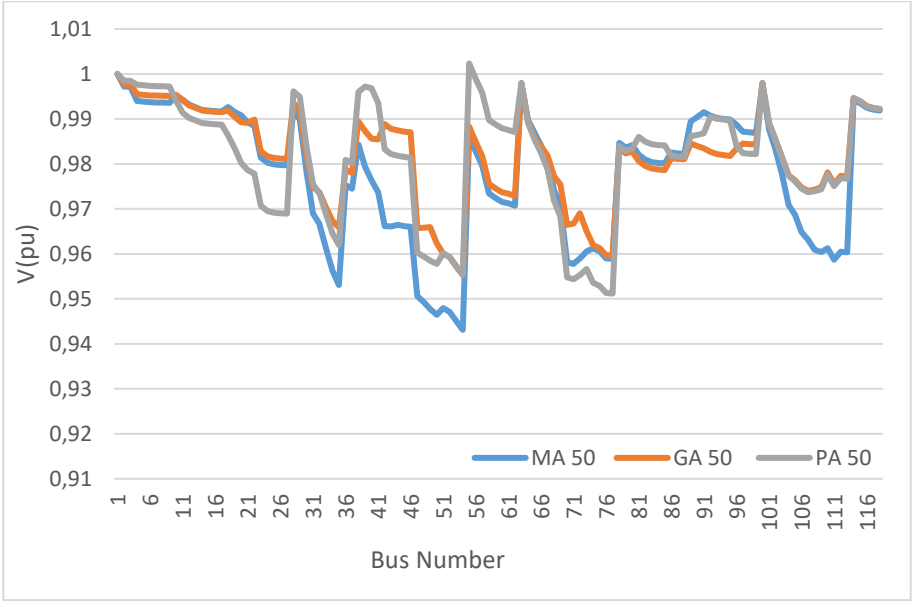

Figure 7: Voltage Profiles of the system with three Algorithms for 50 Iterations

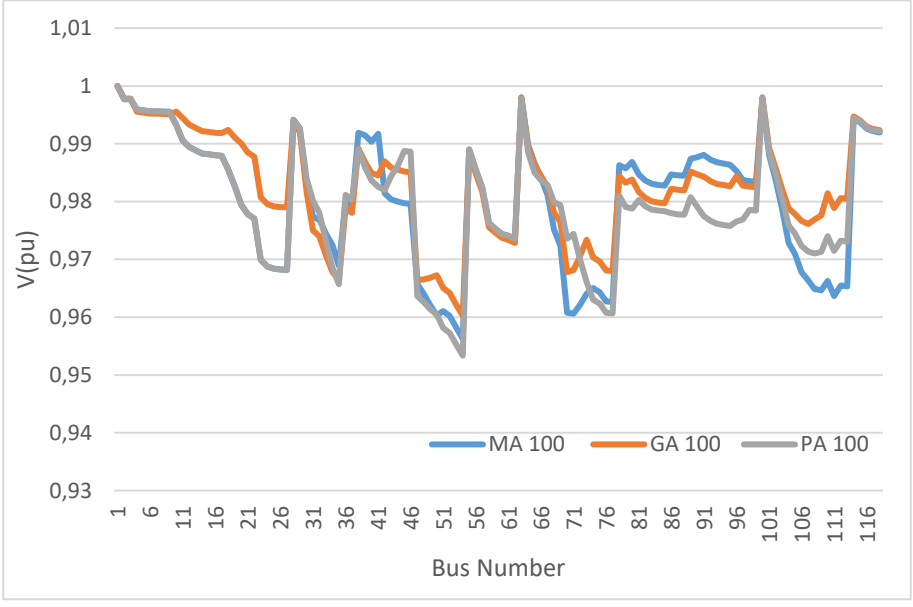

Figure 8: Voltage Profiles of the system with three Algorithms for 100 Iterations

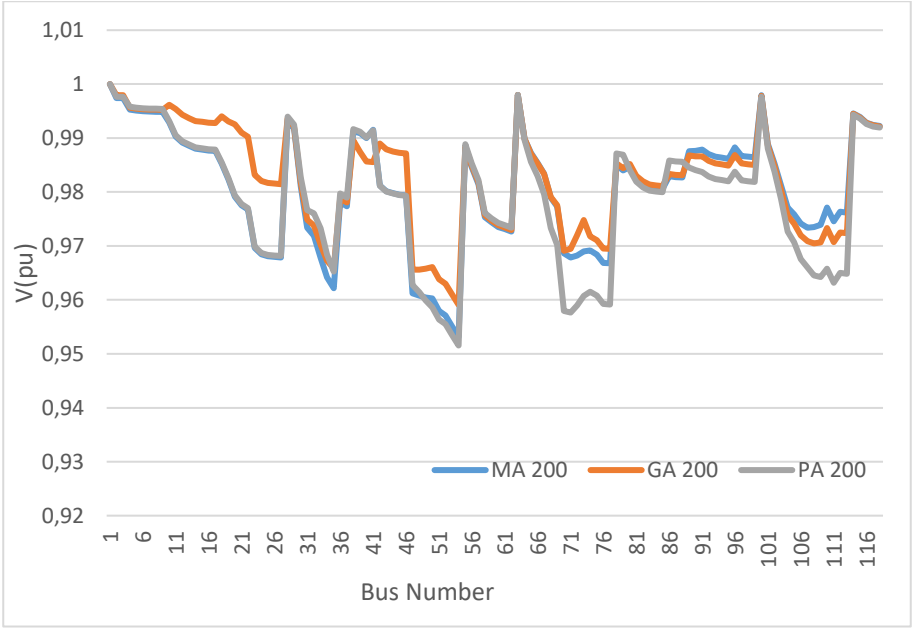

Figure 9: Voltage Profiles of the system with three Algorithms for 200 Iterations

Figure 7 and Figure 8 compares the voltage profiles of the system under three different optimization algorithms: MA, GA, and PA with 50 and 100 iterations, respectively.

Table 2: Location and active Power of Distributed Generators with different Iteration Numbers of the MA

Iteration No.		**50**		**100**		**200**
	Bus	DG Power (MW)	Bus	DG Power (MW)	Bus	DG Power (MW)
Mayfly Algorithm	110	2.2235	80	2.5239	41	21079
	51	1.8228	51	1.4497	50	2.6799
	80	2.2012	34	2.3033	96	1.9556
	74	2.1338	91	2.0365	110	2.9406
	44	2.9495	41	2.0270	70	7.8978
	91	2.3616	110	2.4463	80	2.2442
	20	1.8224	74	2.2689	74	1.8171

Figure 9 illustrates the voltage profiles of a system under three different algorithms (MA, GA, and PA) over 200 iterations. All three algorithms exhibit fluctuations in voltage, but GA demonstrates the most stable performance with

minimal variations. GA appears to be the most effective algorithm in maintaining a stable voltage profile.

When compared to the GA, MA and PA algorithms, the GA algorithm also demonstrates an improvement in voltage stability as the number of iterations increases. However, the performance of different algorithms can vary depending on the specific characteristics of the system and the chosen parameters. Therefore, a comprehensive analysis and comparison are necessary to determine the most suitable algorithm for a particular system.

Table 2 presents the bus locations and active power outputs of distributed generators optimized using the MA for iterations of 50, 100, and 200.

Table 3: Location and active Power of DGs with different Iteration Numbers of the PA

Iteration No.	**50**		**100**		**200**	
	Bus	DG Power (MW)	Bus	DG Power (MW)	Bus	DG Power (MW)
Pelican Algorithm	55	3.4064	71	2.9677	79	2.7455
	81	2.1788	50	2.0558	96	1.7089
	92	2.0385	31	2.7142	33	1.7557
	110	2.9648	81	1.6570	74	2.1882
	40	2.6940	45	9.8472	41	2.0154
	51	2.2610	110	2.7978	110	2.4248
	73	2.0480	98	1.1540	50	1.8078

Table 4: Location and active Power of Distributed Generators with different Iteration Numbers of the GA

Iteration No.	**50**		**100**		**200**	
	Bus	DG Power (MW)	Bus	DG Power (MW)	Bus	DG Power (MW)
Genetic Algorithm	42	1.3856	73	2.6241	96	1.8489
	49	3.1233	110	3.1392	42	1.3845
	80	2.0768	80	2.1832	50	3.0937
	72	2.5778	50	3.1910	110	2.7646
	97	1.6557	42	1.2808	20	1.9783
	22	1.4834	20	1.6095	80	2.3109
	110	2.9867	96	1.6967	73	2.6497

Table 3 shows the locations and active power outputs of distributed generators (DGs) optimized using the PA for iteration numbers 50, 100, and 200. As the iteration increases, the algorithm refines the DG placement and

power allocation, resulting in shifts in bus locations and adjustments to power outputs.

Table 4 provides an analysis of the locations and active power outputs of DGs determined through GA for different iteration numbers (50, 100, and 200). The table highlights the bus numbers where the DGs are placed and their corresponding power outputs in megawatts (MW) for each scenario. GA identifies DGs at buses 42, 49, 80, 72, 97, 22, and 110. The active power of the DGs ranges between 1.3856 MW (bus 42) and 3.1233 MW (bus 49). DG power outputs vary from 1.2808 MW (bus 42) to 3.1910 MW (bus 50) for 100 iterations. The optimal bus locations shift to 96, 42, 50, 110, 20, 80, and 73 and active power values range from 1.3845 MW (bus 42) to 3.0937 MW (bus 50) for 200 iterations.

CONCLUSION

In this study, it is aimed to compare the performances of three different optimization algorithms in determining the optimum connection point and generation power of DG systems. The objective function of the algorithms is to keep the bus voltages in balance and to reduce active power losses.

All three algorithms have been run for the 118-bus system. It has been determined that the GA performed better in terms of reducing active power losses, especially in cases where the number of iterations was low. GA created solutions that provided approximately 3.6% less active power loss for 50 iterations and approximately 1.2% less for 100 iterations compared to the other two algorithms. As the number of iterations increased, the other two algorithms produced similar results to GA. In the GA algorithm, no significant improvement was observed in terms of active power losses with the increase in the number of iterations.

If an evaluation is to be made in terms of voltage profiles, significant improvements were observed in all three algorithms compared to the initial situation. The voltage profile, which could be expressed as >0.87 pu at the beginning, became expressible as >0.94pu. While it is expected that the voltage profile will improve as the number of iterations increases, the obtained graphics do not confirm this expectation. The most important factor here can be shown as the DGs are connected to different buses each time and the

voltage profiles are formed differently according to the connected bus. While improvements are observed in the voltage profile as the number of iterations increases for some buses, there were cases where the opposite effect was observed. Therefore, no finding was reached that increasing the number of iterations will have a definite positive effect on the voltage profile.

REFERENCES

Abdmouleh, Z., Gastli, A., Ben-Brahim, L., Haouari, M., & Al-Emadi, N. A. (2017). Review of optimization techniques applied for the integration of distributed generation from renewable energy sources. Renewable Energy, 113, 266–280. https://doi.org/10.1016/j.renene.2017.05.087

AKDOĞAN, İ., & KOVANCILAR, B. (2022). Avrupa Birliği ve Türkiye'de Çevre Dostu Yenilenebilir Enerji Politikalarının Teşvik Türleri Açısından Değerlendirilmesi. Yönetim ve Ekonomi Dergisi, 29(1), 69–91. https://doi.org/10.18657/yonveek.1004872

Azevedo, B. F., Rocha, A. M. A. C., & Pereira, A. I. (2024). Hybrid approaches to optimization and machine learning methods: a systematic literature review. Machine Learning, 113(7), 4055–4097. https://doi.org/10.1007/s10994-023-06467-x

Babu, P. V., Singh, S., & Singh, S. P. (2017). Distributed generators allocation in distribution system. 2017 IEEE Power & Energy Society General Meeting, 1–5. https://doi.org/10.1109/PESGM.2017.8274197

Basa Arsoy, A., & Perdahçı, C. (2010). Eleketrik Dağitim Sistemlerinde Dağitilmiş Üretim. 1–4.

Dharageshwari, K., & Nayanatara, C. (2015). Multiobjective optimal placement of multiple distributed generations in IEEE 33 bus radial system using simulated annealing. IEEE International Conference on Circuit, Power and Computing Technologies, ICCPCT 2015, 2014, 1–7. https://doi.org/10.1109/ICCPCT.2015.7159428

Dixit, M., Kundu, P., & Jariwala, H. R. (2016). Optimal placement and sizing of DG in Distribution system using Artificial Bee Colony Algorithm. 2016 IEEE 6th International Conference on Power Systems, ICPS 2016, 1–6. https://doi.org/10.1109/ICPES.2016.7584010

Fahim, K. E., Silva, L. C. De, Hussain, F., & Yassin, H. (2023). A State-of-the-Art Review on Optimization Methods and Techniques for Economic Load Dispatch with Photovoltaic Systems: Progress, Challenges, and Recommendations. Sustainability, 15(15), 11837. https://doi.org/10.3390/su151511837

Fanish, R., & Singh Bhadoriya, J. (2007). Optimal Placement of Multi DG in 33 Bus System Using PSO. International Journal of Advanced Research in Electrical, Electronics and Instrumentation Engineering (An ISO, 3297, 3758–3764.

Gopu, P., Naaz, S., & Aiman, K. (2021). Optimal placement of distributed generation using genetic algorithm. Proceedings of the 2021 1st International Conference on Advances in Electrical, Computing, Communications and Sustainable Technologies, ICAECT 2021. https://doi.org/10.1109/ICAECT49130.2021.9392496

Gümüş, T. E., Emiroglu, S., & Yalcin, M. A. (2023). Optimal DG allocation and sizing in distribution systems with Thevenin based impedance stability index. International Journal of Electrical Power & Energy Systems, 144, 108555. https://doi.org/10.1016/j.ijepes.2022.108555

Ismael, S. M., Aleem, S. H. E. A., & Abdelaziz, A. Y. (2018). Optimal sizing and placement of distributed generation in Egyptian radial distribution systems using crow search algorithm. Proceedings of 2018 International Conference on Innovative Trends in Computer Engineering, ITCE 2018, 2018-March, 332–337. https://doi.org/10.1109/ITCE.2018.8316646

Judge, M. A., Franzitta, V., Curto, D., Guercio, A., Cirrincione, G., & Khattak, H. A. (2024). A comprehensive review of artificial intelligence approaches for smart grid integration and optimization. Energy Conversion and Management: X, 24, 100724. https://doi.org/10.1016/j.ecmx.2024.100724

Mandal, P. K. (2023). A review of classical methods and Nature-Inspired Algorithms (NIAs) for optimization problems. Results in Control and Optimization, 13, 100315. https://doi.org/10.1016/j.rico.2023.100315

MathWorks, T. (2020). MATLAB (R2020b). The MathWorks Inc., x.

Niveditha, P., & Sujatha, M. S. (2018). Optimal Allocation and Sizing of DG in Radial Distribution System-A Review. International Journal of Grid and Distributed Computing, 11(6), 49–58. https://doi.org/10.14257/ijgdc.2018.11.6.05

Pesaran H.A, M., Huy, P. D., & Ramachandaramurthy, V. K. (2017). A review of the optimal allocation of distributed generation: Objectives, constraints, methods, and algorithms. Renewable and Sustainable Energy Reviews, 75(November 2016), 293–312. https://doi.org/10.1016/j.rser.2016.10.071

Power system test case archive. (n.d.).

Quirós-Tortós, J., & Fernández-Porras, P. (2017). Controlled Islanding with Special Consideration of Parallel Power System Restoration Constraints. Revista Ingeniería, 27(1), 113. https://doi.org/10.15517/jte.v27i1.26443

Rathore, A., & Patidar, N. P. (2021). Optimal sizing and allocation of renewable based distribution generation with gravity energy storage considering stochastic nature using particle swarm optimization in radial distribution network. Journal of Energy Storage, 35. https://doi.org/10.1016/j.est.2021.102282

S. Blumsack. (2006). Network topologies and transmission investment under electric-industry restructuring. Carnegie Mellon Univ., FL, USA.

Tian, Y., Cai, N., Benidris, M., Bera, A., Mitra, J., & Singh, C. (2017). Sensitivity

guided genetic algorithm for placement of distributed energy resources. 2017 19th International Conference on Intelligent System Application to Power Systems, ISAP 2017, 1–5. https://doi.org/10.1109/ISAP.2017.8071419

Truong, K. H., Nallagownden, P., Elamvazuthi, I., & Vo, D. N. (2020). A Quasi-Oppositional-Chaotic Symbiotic Organisms Search algorithm for optimal allocation of DG in radial distribution networks. Applied Soft Computing Journal, 88, 106067. https://doi.org/10.1016/j.asoc.2020.106067

Varesi, K. (2011). Optimal Allocation of DG Units for Power Loss Reduction and Voltage Profile Improvement of Distribution Networks using PSO Algorithm. World Academy of Science, Engineering and Technology, 60(12–26), 1364–1368. https://doi.org/10.5281/zenodo.1062966

Yu, S., You, L., & Zhou, S. (2023). A review of optimization modeling and solution methods in renewable energy systems. Frontiers of Engineering Management, 10(4), 640–671. https://doi.org/10.1007/s42524-023-0271-3

Zervoudakis, K., & Tsafarakis, S. (2020). A mayfly optimization algorithm. Computers & Industrial Engineering, 145, 106559. https://doi.org/10.1016/j.cie.2020.106559

Zimmerman, R. D., Murillo-Sánchez, C. E., & Thomas, R. J. (2011). MATPOWER: Steady-state operations, planning, and analysis tools for power systems research and education. IEEE Transactions on Power Systems. https://doi.org/10.1109/TPWRS.2010.2051168.

Evaluation of Electric and Magnetic Field Measurements in Isparta Province

Ozlem COSKUN[1,*]

[1]Department of Electrical and Electronics Engineering/Suleyman Demirel University, Turkey
[*](ozlemcoskun@sdu.edu.tr)

ABSTRACT

Nowadays, with the rapidly developing technology, there is a significant increase in electric and magnetic field exposure. Measurements and evaluations are very important to protect people from the possible effects of these areas to which they are unknowingly exposed. The purpose of this study is to make electric and magnetic field measurements at some critical points in Isparta province. Measurement results were compared and evaluated according to international standards. BIOTEST VX0003 device was used for electric field measurements and Fluke 115 True RMS magnetic field device was used for magnetic field measurements. The results were compared with the limit values set by the International Commission on Non-Ionizing Radiation Protection (ICNIRP) for the general public. In electric field and magnetic field measurements; While there is no risk for electric field values according to ICNIRP values, limit values for magnetic field have been exceeded at some points. Devices, tools and equipment that emit electric and magnetic fields should be used with maximum efficiency, but field levels that would harm people's health should not be exceeded.

Keywords – Electric-magnetic field, Electromagnetic pollution, Limit values, Occupational health and safety, ICNIRP

I. INTRODUCTION

One of the biggest problems that arise with today's modern technologies is electromagnetic pollution. The development of telecommunication and the increase in base stations and radio/TV transmitters are among the most important factors that increase electromagnetic pollution in our environment. Electromagnetic fields (EMA) generated by many devices we use every day, such as computers, mobile phones, wireless networks (Wi-Fi), Bluetooth, microwave ovens, disrupt our natural frequency. The effect of electromagnetic radiation on living things does not appear suddenly. It may sometimes take a long time for harmful effects to appear. The most innocent biological effects of electromagnetic radiation (EMR); headaches and migraines, eye irritations and cataracts, loss of appetite, fatigue, dizziness and vomiting, memory loss, depression, and sleep disorders. However, it also has much more serious effects. Tumor formation in the brain, diseases such as Alzheimer's and Parkinson's, eye cancer, epilepsy, stomach pain and digestive disorders, and disorders in the nervous system can be given as examples [1].

Electromagnetic waves are rays emitted from natural and artificial radiation sources. EMR is divided into ionizing radiation and non-ionizing radiation. RF radiation emitted from mobile phones is the type of radiation we are most exposed to in our daily lives. They fall into the non-ionizing radiation class. It

is found in the electromagnetic spectrum at frequencies between approximately 3 kilohertz (3 kHz) and 300 gigahertz (300 GHz) [2].

It is not possible for people to sense the presence of the magnetic field they are exposed to in public places. It is possible for a person to feel it only when exposed to very high magnetic field values. The level of magnetic field that can be felt may vary from person to person. For this reason, the health problems caused by the magnetic field exposed will be noticed in the long term. Today, the most common sources from which the general public is exposed to RF electromagnetic fields are; radio and television broadcasting, telecommunications and wireless communication applications such as base stations for mobile phones, RF identification tagging systems and Wi-Fi. Mobile phone networks worldwide are used for transmission and reception of the Ultra High Frequency (UHF) portion of the RF spectrum. Today, two basic mobile communication technologies are used for mobile communication: Global System (GSM) and Universal Mobile Telecommunication System (UMTS) (3G) [3].

LTE, which entered our lives with 4.5G technology in our country, is another RF EMF source. LTE (high-speed wireless data transfer based on network technologies) coexists with existing technologies that occupy the microwave spectrum [4]. Although wireless systems and base stations operate at frequencies below 300 GHz, within the non-ionizing spectrum, their potential health effects have been the subject of much debate. The International Commission on Non-Ionizing Radiation Protection (ICNIRP), recognized by the World Health Organization (WHO), has established international standards and limits on the effects of EMR on human health. Each country has determined its own borders [5].

Total limit values of the environment according to the regulation on the determination, control and supervision of exposure limit values of electromagnetic field intensity arising from electronic communication devices according to international standards published in the Official Gazette No. 27912 dated April 21, 2011; At GSM 900 MHz, 41.25 V/m for electric field strength (E) and 0.111 A/m for magnetic field strength (H); 58.34 V/m for E and 0.157 A/m for H at GSM 1800 MHz and 61 V/m for E and 0.16 A/m for H at UMTS 2100 MHz [2]. ICNIRP limit values at different frequencies for the general public are given in Table 1. [3].

Table 1. ICNIRP limit values for general public exposure

Frequency	Electric Field E(kV/m)	Magnetic Field (A/m)	Magnetic Flux Density B (T)
1 Hz–8 Hz	5	$3.2x10^4/f^2$	$3.2x10^{-2}/f^2$
8 Hz–25 Hz	5	$4x10^3/f$	$5x10^{-3}/f$
25 Hz–50 Hz	5	$1.6x10^2$	$2x10^{-4}$
50 Hz–400 Hz	$2.5x10^2/f$	$1.6x10^2$	$2x10^{-4}$
400 Hz–3 kHz	$2.5x10^2/f$	$6.4x10^4/f$	$8x10^{-2}/f$
3 kHz–10 MHz	$8.3x10^{-2}$	21	$2.7x10^{-5}$

The city center and nearby areas, schools, medical faculties, shopping malls and university campuses are the areas with the highest human density. Therefore, EMF exposure will increase at frequencies between 3 kHz-300 GHz used in mobile communication systems with the mobile phones used by everyone as a part of modern life. The negative effects of RF radiation exposure on human health have been reported in many studies. There are studies showing that exposure to RF field causes apoptosis, DNA damage and changes in gene expression in cells [6]. For this reason, in such environments where human density is quite high, EMR measurements should be made frequently and electromagnetic pollution maps of the region should be prepared [7], [8].

In this study, it is aimed to contribute to the subject by making electric and magnetic field measurements at some critical points in Isparta province.

II. Electric and Magnetic Field Measurements

In this study, both electric and magnetic field intensity values were measured at ISPARTA TM, ÇÜNÜR 2 DM and M5 downcomer centers. BIOTEST VX0003 device was used for electric field measurements. Since it is a simple and economical device, it is also used for electrical installation control in technical and vocational training. Fluke 115 True RMS device was used for magnetic field measurements. With its simple to use, compact design, the Fluke 115 True RMS digital multimeter provides the perfect answer to general-purpose electrical and electronic testing needs. Fluke 115 displays provide accurate RMS voltage and 600 pixel resolution, continuity and capacity, making them perfect for current readings, rapid verifications and field service use.

Fig. 1 BIOTEST VX0003 electric field measuring device

Fig. 2 Fluke 115 True RMS magnetic field meter

A. ISPARTA TM High Voltage Transformer Center

The first measurements were made at the substation called Isparta TM, belonging to Türkiye Elektrik İletim A.Ş., in the city center of Isparta, at the coordinates of 37°52'43.20"N 30°30'30.25"E. Measurements were made at the high voltage substation, one output of which feeds Burdur and the other feeds Isparta. There are 2 transformers of 100 MVA and 50 MVA in this substation. It has an output of 154 KV.

B. ÇÜNÜR 2 DM Distribution Center

The second measurements were made at the distribution center called ÇÜNÜR DM belonging to Akdeniz Elektrik Dağıtım A.Ş. at the coordinates of 28°28'31"E 41°89'03"N in the city center of Isparta. There is a 250 KWA transformer inside. The transformer converts 34.5 kV medium voltages to 380 V low voltages.

C. M5 Downloader Center

The third measurements were made at the downlinker center called M5 belonging to Akdeniz Elektrik Dağıtım A.Ş. in the city center of Isparta at the coordinates of 28°37'90"E 41°85'72"N. In this step-down center, 34.5 kV medium voltages are converted to 10 kV medium voltages.

III. RESULTS

A. ISPARTA TM High Voltage Transformer Center Findings

Electric field and magnetic field measurements were made by turning around the four sides of the Isparta TM high voltage substation. In this substation, the highest measured value for the electric field was recorded as 200 V/m, and the highest measured value for the magnetic field was recorded as 3 mT.

Fig 3. ISPARTA TM high voltage substation measurements

B. ÇÜNÜR 2 DM Distribution Center Findings

In the measurements made at Çünür 2 DM distribution center, it is 1 m away from the transformer; the electric field was recorded as 400 V/m and the magnetic field was recorded as 0 mT. In the second measurement made for this place, it is 50 cm ahead of the LV distribution panel exit; the electric field was recorded as 0 V/m and the magnetic field was recorded as 2.4 mT.

Fig 4. ÇÜNÜR 2 DM distribution center measurements

D. M5 Downloader Center Findings

In the first measurement made for the M5 step-down center, the 5 MVA transformers was 1.5 m ahead of the bushing; the electric field was recorded as 400 V/m and the magnetic field was recorded as 2.3 mT. In the second measurement, 2.5 m ahead of the transformer; the electric field was recorded as 100 V/m and the magnetic field was recorded as 0 mT.

Fig 5. M5 downcomer center measurements

IV. CONCLUSION

In the electric field and magnetic field measurements made by rotating on all four sides of Isparta TM high voltage substation; while there is no risk for electric field values according to ICNIRP values, limit values for magnetic field have been exceeded. In the measurements made at Çünür 2 DM distribution center, while there was no risk in the electric and magnetic field values at a distance of 1 m from the transformer, the limit values were exceeded in the magnetic field values at a distance of 0.5 m. There is no risk in electric field values. In the first measurements made for the M5 step-down center, the 5 MVA transformer was 2.5 m ahead of the bushing; While there was no risk in the electric and magnetic field values, the limit values in the magnetic field values were exceeded 1.5 m ahead of the transformer. There is no risk in electric field values.

It is indisputable that electromagnetic fields generated during the transmission and use of electrical energy has possible effects on the environment and human health. Especially people who are exposed to the effects of electromagnetic fields due to professional obligations may face serious health problems as a result of long-term exposure. Studies evaluating the health effects of EMA have focused on certain diseases that are predicted to be affected. The relationship between EMF and childhood leukemia has been clearly demonstrated. As a result of the development of today's electrical, electronic and communication technologies, people are consciously or unconsciously exposed to electromagnetic field radiation. It is not possible to completely avoid this exposure, but necessary efforts can be made to keep exposure to a minimum level by raising public awareness on this issue.

REFERENCES

[1] K. A. Ansal, D. S. Jose, R. K. Rajan, Review on biological effect of electromagnetic radiation. *In 2018 International Conference on Circuits and Systems in Digital Enterprise Technology (ICCSDET)* (pp. 1-5). IEEE, 2018.

[2] O. Sogut, E. Kucukonder, O. Sahin, Measurement of electromagnetic pollution along Alparslan Türkeş and Hanefi Mahçiçek boulevards in Kahramanmaraş. *Kahramanmaraş Sütçü İmam University Journal of Engineering Sciences,* 20(3), 84-95, 2017.

[3] O. Cerezci, S. C. Yener, Electromagnetic Pollution in Our Environment and Its Effects on Our Health *In 3rd International Symposium on Environment and Morality (ISEM2016)*, Antalya, 2016.

[4] P. Gajšek, P. Ravazzani, J. Wiart, J. Grellier, T. Samaras, G. Thuróczy, Electromagnetic field exposure assessment in Europe radiofrequency fields (10 MHz–6 GHz). *Journal of exposure science and environmental epidemiology*, *25*(1), 37, 2015.

[5] C. Kurnaz, An emprical modelling of electromagnetic pollution on an university campus. *The Applied Computational Electromagnetic Society Express Journal*, *1*(2), 76-79, 2016.

[6] M. Z. Tuysuz, H. Kayhan, A. S. Y. Saglam, E. U. Bagriacik, M. Yagci, A. G. Canseven. Effect of radiofrequency electromagnetic field resulting from mobile phone exposure on apoptosis. *Journal of Harran University Faculty of Medicine*, *16*(1), 123-129, 2019.

[7] T. Karadag, A. R. Ozdemir, T. Abbasov, Measuring and mapping long-term and continuous electromagnetic pollution levels in a selected pilot region. *Gazi University Journal of Science, Part:C, Design and Technology*, 2(3):239-246, 2014.

[8] J. C. Lin, Human exposure to RF, microwave, and millimeter-wave electromagnetic radiation [Health Effects]. *IEEE Microwave Magazine*, *17*(6), 32-36, 2016.